

A Surface Wave Model for Coupling with Numerical Ocean Circulation Models

GEORGE L. MELLOR

Atmospheric and Oceanic Sciences Program, Princeton University, Princeton, New Jersey

MARK A. DONELAN

Rosenstiel School of Marine and Atmospheric Sciences, University of Miami, Miami, Florida

LIE-YAUW OEY

Atmospheric and Oceanic Sciences Program, Princeton University, Princeton, New Jersey

(Manuscript received 30 April 2007, in final form 15 February 2008)

ABSTRACT

A surface wave model is developed with the intention of coupling it to three-dimensional ocean circulation models. The model is based on a paper by Mellor wherein depth-dependent coupling terms were derived. To be compatible with circulation models and to be numerically economical, this model is simplified compared to popular third-generation models. However, the model does support depth and current refraction, deep and shallow water, and proper coupling with depth-variable currents.

The model is demonstrated for several simple scenarios culminating in comparisons of model calculations with buoy data during Hurricane Katrina and with calculations from the model Simulating Waves Nearshore (SWAN); for these calculations, coupling with the ocean was not activated.

1. Introduction

This paper follows a paper by Mellor (2003, hereafter M03), which, however, has been revised (Mellor 2008); the revisions did change Eqs. (6)–(8) below but do not affect any calculated results in this paper since coupling with an ocean has not been activated. The phase-averaged, wave–current equations of motion were extended to the third vertical dimension. In much of the literature (e.g., Phillips 1977), the wave interacting continuity and momentum equations were, a priori, vertically integrated, rendering them unsuitable for coupling with depth-dependent numerical ocean circulation models. Now, as a consequence of (the revised) M03, it is possible to couple three-dimensional circulation models with wave models; the coupling includes depth-dependent wave radiation stress terms, Stokes drift, vertical transfer of wave-generated pressure transfer to the mean momentum equation, wave dissipation as a source term in the turbulence kinetic energy equation,

and mean current advection and refraction of wave energy.

There exist functional third-generation wave models such as Wave Model (WAM) (WAMDI Group 1988; Komen et al. 1994), WAVEWATCH (Tolman 1991), and Simulating Waves Nearshore (SWAN) (Booij and Holthuijsen 1999). However, for many users, these models cannot practically be coupled to circulation models. Circulation models invoke four independent variables—three horizontal and vertical coordinates and time, x, y, z, t —whereas the wave models use five independent variables—two horizontal coordinates and time, x, y, t , plus the wave propagation angle, θ , and frequency, σ . Consider frequency as the additional variable with, say, 30 numerically discrete, frequency bins; then add time for the computation of nonlinear wave–wave interaction and the integration of various properties including the new coupling terms (M03; Mellor 2005). Thus, one is faced with about a two orders of magnitude increase in computational effort over that required by circulation models cum sole. This is the actual experience obtained with an operational model of the New York Harbor coastal and estuarine region (www.stevens.edu/maritimeforecast/). The model builders (A. Blumberg 2006, personal communication)

Corresponding author address: Prof. George Mellor, Sayre Hall, Forrestal Campus, Princeton University, Princeton, NJ 08544-0710.

E-mail: glmellor@princeton.edu

found that for the same horizontal grid and length of run, the SWAN model required 86 times the computer run time compared to the circulation model, in this case the Princeton Ocean Model (POM); the two models were not coupled. Circulation model applications are typically executed with marginal horizontal resolution commensurate with available computational resources so that the two orders of magnitude increased computational time will be prohibitive for many coupled circulation–wave model applications.

In the literature, one finds that Mastenbroek et al. (1993) did couple the WAM model to a surge model and was able to incorporate the vertically integrated, wave radiation stress terms into the shallow-water continuity and momentum equations; this was followed by a similar paper by Ozer et al. (2000) that included tides and surges. Zhang and Li (1997) coupled a wave equation (without frequency and directional dependence) to a three-dimensional barotropic ocean model. They did solve a separate transport equation for wavenumber and, thus, frequency. A simple eddy viscosity parameterization allowed wind stress momentum transfer into the water column. Xie et al. (2001) ran POM and WAM simultaneously and coupled the wave and circulation models only through surface and bottom stress roughness terms; they performed a series of 1-day runs to determine the effect of wave-enhanced stresses on the currents. Moon (2005) combined POM and WAVEWATCH III; and a wave stress was obtained from an integral of the wave spectrum (see relevant discussion in sections 5 and 8 below). Also, wave dissipation produced a turbulence source term for the Mellor and Yamada (1982) turbulence closure model (Mellor and Blumberg 2004). All of the above papers were for deep water, for limited regions, and for limited run times. Since vertically dependent radiation stress terms were not available, they were excluded from all wave energy and momentum equations, except for the vertically integrated surge model. Surface-weighted Doppler velocities derived from depth-dependent currents and pressure transfer of wind stress were also excluded.

Thus, there is a need for a numerically practical wave model that can be coupled to three-dimensional, time-dependent circulation models for long-term simulations and high-resolution, regional, basin, or global domains. The wave model could supply estimates of wave heights (useful, e.g., in parameterizing wind drag coefficients as well as other estimates of sea state; see Janssen et al. 2004) and depth-dependent wave radiation stress terms for the momentum equation, which would feed back depth-dependent velocity fields to the wave energy equation.

A possible candidate is the simple Great Lakes En-

vironmental Research Laboratory (GLERL) model [Schwab et al. (1984), originally devised by Donelan (1977)], which is used by at least two regional operational models known to us. Despite its simplicity the GLERL model has been shown to be relatively consistent with observations in several studies (Schwab et al. 1984; Lin et al. 2002). However, that model precludes swell, shallow-water effects, refraction, explicit wave dissipation, and exchange of current and Stokes drift momentum.

Here, to include these attributes, we have developed a model that borrows a feature of the GLERL wave model and other models (SWAMP Group 1985) in that the energy distribution in frequency space is parameterized using the spectrum by Donelan et al. (1985, henceforth DHH85), and which contains elements of the Joint North Sea Wave Project (JONSWAP) spectrum (Hasselmann et al. 1973). The model avoids dealing with the wave–wave interaction process (the process is compensated by the specified spectral shape), and has the same level of complexity as circulation models whose four independent variables are x, y, z, t ; the present wave model also has four independent variables, x, y, θ, t ; the wave propagation angle, θ , will account for refraction due to bottom depth and current variations. Frequency is also dependent on x, y, θ, t ; in the wind-driven portions of θ , the transport equation for frequency is forced by and asymptotes in time to the peak frequency of the parameterized spectrum; otherwise, the frequency is advected as swell. There is some similarity with this approach and the HISWA model (Holthuijsen et al. 1989) in that the main dependent variables are wave angle–dependent energy and frequency. The model is meant for stationary calculations for nearly fixed mean direction—the grid is oriented in the mean wave direction, say toward a coastline or a harbor—and is numerically not applicable to arbitrary basins or wind directions. Source and sink terms are derived differently than described below.

The numerical wave model code is composed of subroutines; the main subroutine can be conveniently called by a circulation model, and will approximately require the same computer resources as a circulation model.

Another motivation for the model is to directly confront unresolved research issues. For example, in M03, it was seen that some or all of the momentum transfer to the immediately underlying surface boundary layer is due to pressure transfer; surface boundary layer models currently assume that momentum transfer into the water column is entirely due to turbulence mixing.

Constraining to a specific spectral shape will, of course, not always conform to measured spectra; lost

accuracy in, say, the prediction of significant wave height and other integral wave properties remains to be determined. (However, see section 9 below.)

We face a persistent and common dilemma: whether to define wave age as c_p/U_{10} , c_p/u_* , or $c_p/U_{p,\lambda/2}$, where c_p is the phase speed at the peak of the wave spectrum, U_{10} is the wind speed at 10 m above the sea surface, u_* is the friction speed, and $U_{p,\lambda/2}$ is the wind speed at a half-wavelength above the sea surface at the peak frequency. Since the main parameter in the spectrum according to DHH85 is c_p/U_{10} , we will mostly follow the same practice. [However, as discussed below, c_p/U_{10} will be converted to $g/(\sigma_p U_{10})$, an equality for deep water but not for shallow water.] Alves et al. (2003) offer evidence that c_p/U_{10} is the preferable wave age descriptor and from a practical point of view u_* is difficult to measure, but the issue does remain uncertain.

In this paper, we develop the wave model cum sole, a necessary precursor to coupling a wave model to a three-dimensional circulation model.

Let $E_{\sigma,\theta} = E_{\sigma,\theta}(x, y, t, \sigma, \theta)$ be the directional spectrum of kinematic energy (divided by the water density, ρ_w), a function of x, y, t —a point in horizontal space and time—and σ, θ , the frequency and wave direction. Henceforth, the arguments x, y, t will be deleted. In this paper we calculate only

$$E_\theta \equiv \int_0^\infty E_{\sigma,\theta} d\sigma, \tag{1a}$$

and since the kinetic and potential energies are equal,

$$E_T = g\overline{\eta^2} = \int_{-\pi}^\pi E_\theta d\theta \tag{1b}$$

is the total kinematic wave energy per unit surface area: the product of the gravity constant and phase-averaged, squared wave elevation summed over all frequencies and directions. We restrict our attention to surface gravity waves (i.e., wavelengths in excess of about 10 cm).

In section 2, the linear wave relations are reviewed. The model is developed in sections 3–7. An array of canonical tests is executed in section 8. The model is then applied to the Gulf of Mexico during the period of Hurricane Katrina; the path of the hurricane passed near six National Data Buoy Center (NDBC) buoys to which model calculations are compared. Parallel calculations and comparisons are made using the SWAN model. Section 10 is a summary. Appendixes contain some detailed information.

2. Monochromatic unidirectional equations and definitions

We first define terms for a monochromatic unidirectional wave field pursuant to dealing with spectra as a

function of frequency and wave propagation angle. Thus,

$$\begin{aligned} \omega &= \sigma + k_\alpha u_{A\alpha}, \\ \sigma^2 &= gk \tanh kD, \\ c &= \sigma/k, \end{aligned} \tag{2a, b, c}$$

where $k_\alpha = k(\cos\theta, \sin\theta)$ is the wavenumber vector and $k = |k_\alpha|$; θ is the wave propagation direction relative to the eastward direction; σ is the intrinsic frequency; the Doppler velocity, $u_{A\alpha}$, will be defined below; c is the phase speed; g is the gravity constant; $D = h + \hat{\eta}$ is the water column depth where $\hat{\eta}$ is the mean (phase averaged) surface elevation and h is the bottom depth. The group velocity is

$$c_g = \frac{\partial\sigma}{\partial k} = cn, \tag{3a}$$

$$n = \frac{1}{2} + \frac{kD}{\sinh 2kD}, \tag{3b}$$

$$c_{g\alpha} = \frac{k_\alpha}{k} c_g. \tag{3c}$$

For the present wave model, the dispersion relation (2b) is initially solved iteratively, inverted, and cast in the form $kD = f_1(\sigma^2 D/g)$; and from (3b), $n = f_2(\sigma^2 D/g)$. A lookup table with interpolation comprises a subroutine in the numerical code.

As cited in Komen et al. (1994), the refraction speed is $c_\theta = -|\nabla_n \omega \times \mathbf{k}|/k^2$, where ω is obtained from (2a). Working out the vector algebra (Golding 1978) yields

$$\begin{aligned} c_\theta &= \frac{g}{2c \cosh^2 kD} \left(\sin\theta \frac{\partial D}{\partial x} - \cos\theta \frac{\partial D}{\partial y} \right) \\ &+ \frac{k_\alpha}{k} \left(\sin\theta \frac{\partial u_{A\alpha}}{\partial x} - \cos\theta \frac{\partial u_{A\alpha}}{\partial y} \right). \end{aligned} \tag{4}$$

Before defining more terms, useful combinations of hyperbolic sines and cosines are

$$F_{SS} = \frac{\sinh kD(1+s)}{\sinh kD}, \tag{5a}$$

$$F_{CS} = \frac{\cosh kD(1+s)}{\sinh kD} \tag{5b}$$

$$F_{SC} = \frac{\sinh kD(1+s)}{\cosh kD}, \tag{5c}$$

$$F_{CC} = \frac{\cosh kD(1+s)}{\cosh kD}. \tag{5d}$$

The “sigma” variable is $s = (z - \hat{\eta})/D$ (reserving σ for frequency) so that $D(1 + s) = D + z - \hat{\eta}$.

A Doppler (or advective) velocity is required for the wave energy equation and is

$$u_{\Lambda\alpha} = kD \int_{-1}^0 U_{\alpha} [(F_{CS}F_{CC} + F_{SS}F_{SC})/2 + F_{CS}F_{SS}] ds, \quad (6)$$

where $U_{\alpha} = U_{\alpha}(x, y, s, t)$ is the ocean current plus the Stokes drift. The weight factor in the square brackets is significantly nonzero only in the wave portion of the water column. Equation (6) is from M03 (and its revision cited in section 1).

The wave radiation stress terms are

$$\frac{\partial E_{\theta}}{\partial t} + \frac{\partial}{\partial x_{\alpha}} [(\bar{c}_{g\alpha} + \bar{u}_{\Lambda\alpha})E_{\theta}] + \frac{\partial}{\partial \theta} (\bar{c}_{\theta}E_{\theta}) + \int_{-1}^0 \bar{S}_{\alpha\beta} \frac{\partial U_{\alpha}}{\partial x_{\beta}} D ds = S_{\theta\text{in}} - S_{\theta\text{Sdis}} - S_{\theta\text{Bdis}}. \quad (8)$$

The horizontal coordinates are denoted by $x_{\alpha} = (x, y)$. The overbars represent spectral averages (and differ from the phase averaging usage in M03). The first two terms on the left of (8) determine the propagation of wave energy in time and horizontal space whereas the third term is the refraction term accounting for the change in direction of wave energy propagation. The last term on the left of (8) represents energy exchange with the mean velocity energy equation. All of the terms in (8) are functions of θ : $S_{\theta\text{in}}$ is the wave energy source term dependent on wind properties; $S_{\theta\text{Sdis}}$ and

$$S_{\alpha\beta} = kE \left(\frac{k_{\alpha}k_{\beta}}{k^2} F_{CS}F_{CC} - \delta_{\alpha\beta}F_{SC}F_{SS} \right) + \delta_{\alpha\beta}E_D, \quad (7)$$

where a modified delta function, E_D , is defined such that

$$E_D = 0 \text{ if } s \neq 0 \quad \text{and} \quad \int_{-1}^0 E_D D ds = E/2.$$

3. The wave energy equation and the specified spectrum

After integrating the full spectral equation (a function of frequency and wave angle) with respect to frequency, we arrive at

$S_{\theta\text{Bdis}}$ are wave dissipation due to wave processes at the surface and bottom, respectively. All terms are kinematic (i.e., energy terms are divided by water density). Thus the atmospheric work done on the water is $\rho_w S_{\theta\text{in}}$, where ρ_w is the seawater density. The terms, $\bar{c}_{g\alpha}$, \bar{c}_{θ} , $\bar{u}_{\Lambda\alpha}$ and $\bar{S}_{\alpha\beta}$, differ from their counterpart terms in section 2 in that they have been spectrally averaged as described in section 4.

Following DHH85 and for the wind-driven part of the spectrum, we stipulate

$$E_{\sigma,\theta} = \Phi(\sigma, U_c/c_p) \frac{\beta}{2} \text{sech}^2[\beta(\theta - \bar{\theta})], \quad (9a)$$

$$\Phi(\sigma, U_c/c_p) = \alpha g^3 \sigma^{-4} \sigma_p^{-1} \exp \left[- \left(\frac{\sigma}{\sigma_p} \right)^{-4} \right] \gamma^{\exp[-(\sigma - \sigma_p)^2 / (2\sigma_{pw}^2 \sigma_p^2)]}. \quad (9b)$$

Frequency is σ and σ_p is the peak frequency where $E_{\sigma,\theta}$ is maximum; θ is the wave propagation direction; $\bar{\theta}$ is the mean wave propagation angle [see (24)]. Deferring to DHH85 (535–538) or Komen et al. (1994, p. 187) for details, $\beta = \beta(\sigma/\sigma_p)$ and the other parameters in (9) are wave age dependent such that $\alpha = \alpha(U_c/c_p)$, $\gamma = \gamma(U_c/c_p)$, $\sigma_{pw} = \sigma_{pw}(U_c/c_p)$, and $U_c = U_{10} \cos(\theta_w - \bar{\theta})$; U_{10} is the wind speed evaluated at the 10-m height and θ_w is the wind angle. The observations in DHH85 showed that $\bar{\theta}$ can differ from θ_w . In this model building process, we will use (9a) and (9b) as a weighting function where, however, retention or neglect of the difference between

θ_w and $\bar{\theta}$ makes little difference in the calculated results; thus we set $U_c = U_{10}$. Using (9a) and (9b), various spectrally weighted averages were obtained by numerical integration. Following Terray et al. (1996) and Banner (1990), the spectra were extended beyond $3.5\sigma_p$ by appending a σ^{-5} tail to $20\sigma_p$, whence the integration was terminated.

Peak frequency

Following DHH85, to obtain the peak frequency for wind-driven waves, numerical integration of (9a) and (9b) over σ and θ yields $\sigma_p^4 E_{\text{TW}}/g^3$ as a function of

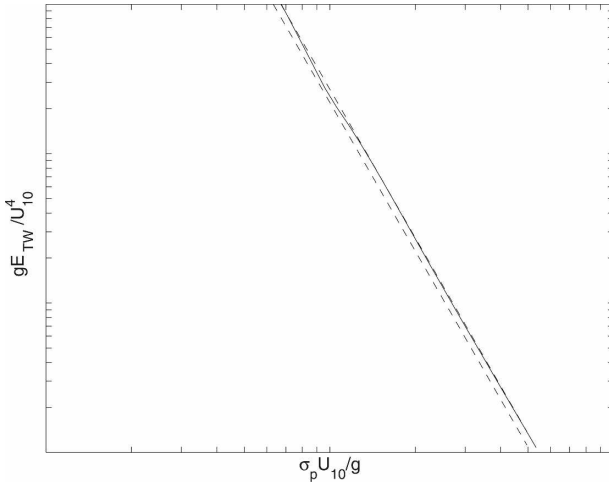


FIG. 1. The inverse wave age dependence of the relation between peak frequency, total wave energy, and wind speed. The solid line is calculated from (9) whereas the dashed line is from (10) with $C_\sigma = 0.0022$.

U_{10}/c_p , which, for deep water, equals $\sigma_p U_{10}/g$. It is believed (Hwang and Wang 2004) that the latter term provides results that are less dependent on depth than is the former (for waves propagating onto a beach with no currents and light winds, $\sigma_p U_{10}/g \equiv \text{constant}$ whereas $U_{10}/c_p \rightarrow \infty$ as $k_p D \rightarrow 0$). We define E_{TW} as the integral of the portion of E_θ that is wind driven; until we later encounter the need to separate swell from wind-driven portions of E_θ , $E_{TW} = E_T$.

The calculated integral from (9a) and (9b) is provided nondimensionally in Fig. 1 as a solid line. By analyzing data from Lake St. Clair, Donelan et al. (1992) found that

$$E_{TW}g/U_{10}^4 = C_\sigma(U_{10}\sigma_p/g)^{-3.3}, \quad (10)$$

where $C_\sigma = 0.0022$. This formula also agrees quite nicely with a plot by Hwang and Wang (2004, their Fig. 5c) for the same nondimensional variables. Their study included fetch-limited and duration-limited data. Young (2006) analyzed hurricane data from a measurement site located off the northwest coast of Australia. He found good agreement with (10); citing DHH85, he noted, “the fact that both the one-dimensional and directional spectra are very similar to spectra reported under simple unidirectional winds is interpreted as being the result of the shape stabilization effects of nonlinear interactions.” Refer to these papers to see data scatter around the average.

Equation (10) can also be written as

$$U_{10}\sigma_p/g = (C_\sigma U_{10}^4/gE_{TW})^{0.303} \quad (11)$$

and will be used to obtain σ_p . Next a small modification of (11) is possible by noting that dimensional analysis

yields $\text{fcn}[E_{TW}g/U_{10}^4, U_{10}\sigma_p/g, (E_{TW}/g)^{1/2}/z_{10}] = 0$, where the length scale, $(E_{TW}/g)^{1/2} = H_S/4$, divided by $z_{10} = 10$ m is now added to the group of relevant nondimensional variables. Here $H_S = 4(E_T/g)^{1/2}$ is the significant wave height (Longuet-Higgins 1952). [Note that z_{10} is important in the conventional velocity-dependent drag coefficient $C_D = C_D(U_{10})$, which in dimensionless terms should be—but usually is not—written $C_D = C_D(U_{10}/\sqrt{z_{10}g})$.]

The possibility that $(E_{TW}/g)^{1/2}/z_{10}$ might be significant led to regression analyses using buoy data discussed in section 9 and model data comparisons. The results showed a weak but nevertheless discernable dependence such that replacing the constant in (11) with $C_\sigma = 0.0015 + 0.0079(E_{TW}/g)^{1/2}/z_{10}$ resulted in some improvement in model wave periods for hurricane-scale winds in comparison with the buoy data discussed in section 9. For intermediate wind, $C_\sigma \equiv 0.0022$.

4. Spectrally averaged terms

Next we deal with terms that are predominantly independent of wave angle. For example,

$$\frac{\bar{c}_g}{c} = \frac{\int_0^\infty (c_g/c)E_{\sigma,\theta} d\sigma}{\int_0^\infty E_{\sigma,\theta} d\sigma} \quad (12a)$$

is, strictly speaking, a function of θ . However, a common approximation is that $E_{\sigma,\theta} = \text{fcn}(\theta)E_\sigma$. An examination of (9) shows that the two independent variables are not exactly separable, but nevertheless trials using (12a) show that the approximation is sufficiently accurate such that

$$\frac{\bar{c}_g}{c} = \frac{\int_0^\infty (c_g/c)E_\sigma d\sigma}{\int_0^\infty E_\sigma d\sigma}, \quad (12b)$$

where $E_\sigma = \int_{-\pi/2}^{\pi/2} E_{\sigma,\theta} d\theta$. Similarly, integrations were carried out for other terms such that, in place of (4), (6), and (7), we have

$$\bar{c}_\theta = \frac{gF_{c\theta}}{2c \cosh^2 kD} \left(\sin\theta \frac{\partial D}{\partial x} - \cos\theta \frac{\partial D}{\partial y} \right) + \frac{k_\alpha}{k} \left(\sin\theta \frac{\partial \bar{u}_{\Lambda\alpha}}{\partial x} - \cos\theta \frac{\partial \bar{u}_{\Lambda\alpha}}{\partial y} \right), \quad (13a)$$

$$\bar{u}_{\Lambda\alpha} = \int_{-1}^0 U_\alpha F_3 ds, \quad (13b)$$

$$\bar{S}_{\alpha\beta} = k_p E_\theta \left(\frac{k_\alpha k_\beta}{k^2} F_1 - \delta_{\alpha\beta} F_2 \right) + \delta_{\alpha\beta} E_{D\theta}, \quad (13c)$$

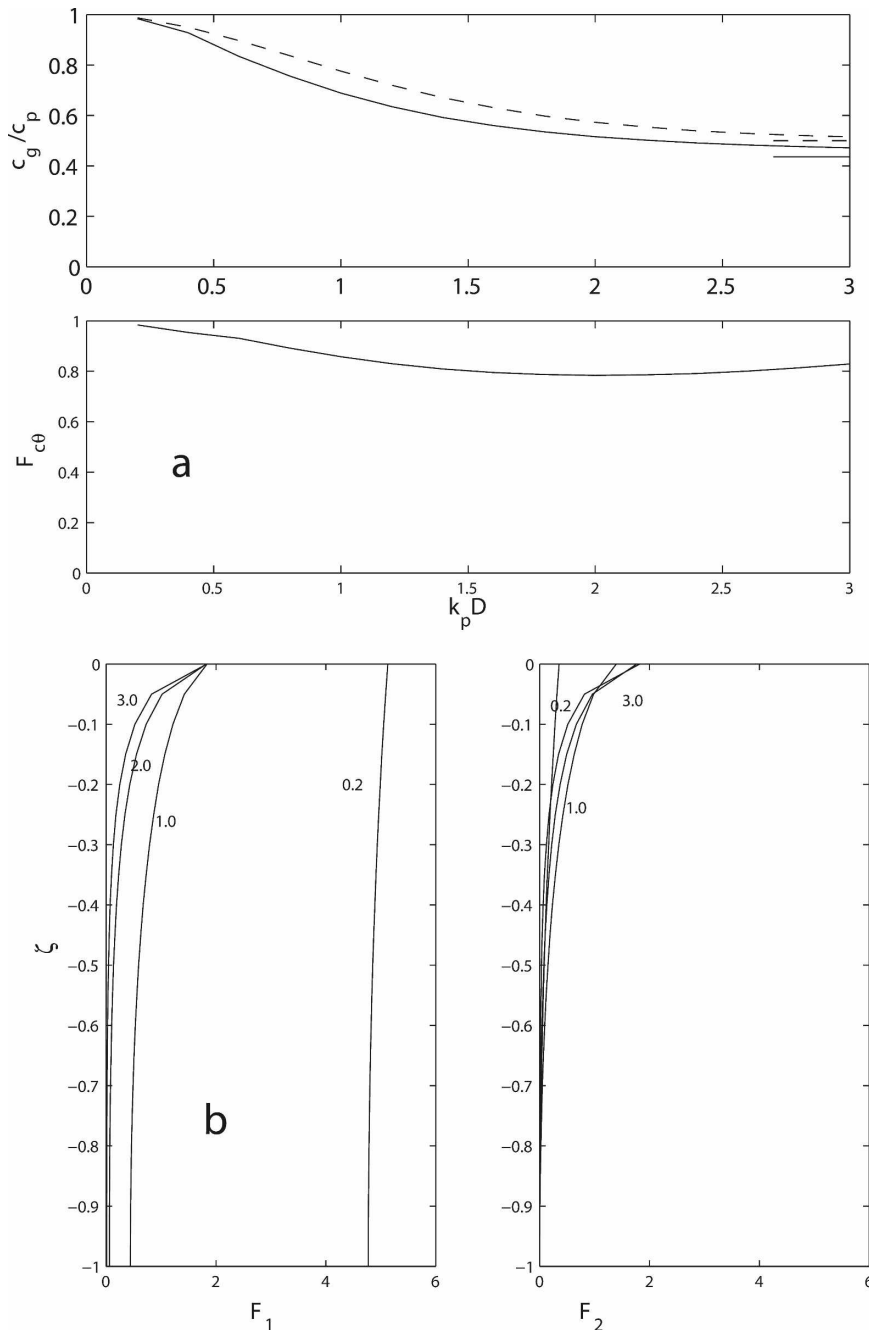


FIG. 2. (a) The solid curves are spectrally weighted values of (top) \bar{c}_g/c_p and (bottom) $F_{c\theta}$ as functions of $k_p D$. The dashed curve is from (3b). The short horizontal lines are asymptotes as $k_p D \rightarrow \infty$. Wave age dependencies are small and are ignored in the model. (b) Spectrally weighted values of (left) F_1 and (right) F_2 for $k_p D = 0.2, 1.0, 2.0$, and 3.0.

and, similarly to (7), we have

$$E_{D\theta} = 0 \text{ if } \zeta \neq 0 \quad \text{and} \quad \int_{-1}^0 E_{D\theta} D \, d\zeta = E_\theta/2.$$

In Fig. 2a, \bar{c}_g/c and $F_{c\theta}$ are plotted as functions of $k_p D$.

These variables are also dependent on inverse wave age, but the dependence is weak (a few percent) and will be neglected henceforth. For comparison, Eq. (3b) where kD is replaced by $k_p D$ is also plotted in Fig. 2a.

The F_n functions in (13b) and (13c), related to the

definitions (5), are explicitly defined in appendix A and are functions of s and $k_p D$ as shown in Fig. 2b for $\sigma_p U_{10}/g = 2$. The variations with respect to inverse wave age are small (in the range, $1 < \sigma_p U_{10}/g < 5$, mostly less than $\pm 5\%$ with a very few values near

$\pm 10\%$) and henceforth are neglected. Appendix A provides further information.

The wave-current interaction terms in (8) are complicated and an explicit record of the terms prior to coding is useful. Thus,

$$\int_{-1}^0 \bar{S}_{\alpha\beta} \frac{\partial U_\alpha}{\partial x_\beta} D ds = E_\theta D \left[\cos^2 \theta \int_{-1}^0 \frac{\partial U}{\partial x} F_1 ds - \int_{-1}^0 \frac{\partial U}{\partial x} F_2 ds + \cos \theta \sin \theta \int_{-1}^0 \left(\frac{\partial U}{\partial y} + \frac{\partial V}{\partial x} \right) F_1 ds + \sin^2 \theta \int_{-1}^0 \frac{\partial V}{\partial y} F_1 ds - \int_{-1}^0 \frac{\partial V}{\partial y} F_2 ds \right]. \tag{14}$$

Recall that $U_\alpha = (U, V)$ is the ocean current plus Stokes velocities.

5. Wind growth source term

The friction velocity is obtained from the well-known relations

$$u_{*a}^2 = C_D |\mathbf{U}_{10} - \mathbf{U}(0)|^2, \\ C_D = \left[\frac{\kappa}{\ln(10 \text{ m}/z_0)} \right]^2, \\ z_0 = 1.38 \times 10^{-4} H_S \left(\frac{\sigma_p U_{10}}{g} \right)^{2.66}, \tag{15a, b, c}$$

where $\mathbf{U}_{10} - \mathbf{U}(0)$ is the vector difference between the 10-m wind velocity and the surface ocean current. The airside and waterside friction velocities are u_{*a} and u_{*w} , such that $\rho_w u_{*w}^2 = \rho_a u_{*a}^2$; $\rho_w/\rho_a = 860$ is the water to air density ratio, (15c) is from Donelan (1990), and $H_S = 4(E_T/g)^{1/2}$ is the significant wave height.

We next obtain $S_{\theta in}$, which can be written

$$S_{\theta in} = \int_0^\infty B_{\sigma, \theta} E_{\sigma, \theta} d\sigma; \tag{16}$$

$E_{\sigma, \theta}$ is given by (9a) and (9b). The wave growth according to Donelan (1999) is

$$B_{\sigma, \theta} = 0.28 \frac{\rho_a}{\rho_w} |U(\lambda/2) \cos(\theta - \theta_w)/c - 1| [U(\lambda/2) \cos(\theta - \theta_w)/c - 1] \sigma, \tag{17}$$

where $U(\lambda/2)$ is the wind speed evaluated at the half-wavelength height. Equation (17) has some similarity to an expression from Janssen (1989) although he used the airside friction velocity u_{*a} instead of $U(\lambda/2)$; the latter can be obtained from U_{10} using the law of the wall according to $U(\lambda/2)/U_{10} = \ln(\lambda/2z_0)/\ln(10 \text{ m}/z_0)$, where $\lambda = 2\pi g \sigma^{-2} \tanh kD$. Sample plots of $E_\sigma = \int_{-\pi}^\pi E_{\sigma, \theta} d\theta$ using (9) and $B_\sigma = \int_{-\pi}^\pi B_{\sigma, \theta} d\theta$ from (17) are shown in Fig. 3. Thus it is seen that the wind source

term is shifted toward large frequencies since, for deep water, $c^{-1} = \sigma/g$.

Equation (16) was integrated to obtain the so-called spreading function $f_{spr} = S_{\theta in}/S_{Tin}$, where $S_{Tin} = \int_{-\pi/2}^{\pi/2} S_{\theta in} d\theta$; the results are plotted in Fig. 4. The dashed line is

$$f_{spr} \equiv \begin{cases} \frac{\beta}{2} \text{sech}^2[\beta(\theta - \theta_w)]; & |\theta - \theta_w| \leq \pi/2 \\ 0; & |\theta - \theta_w| > \pi/2 \end{cases} \tag{18a}$$

for $\beta = 2.2$. The spreading function is similar to that in (9) after replacing $\bar{\theta}$ with θ_w since the weighting function, used to find a local wave energy source term, $S_{\theta in}$, should depend on the local wind direction. As will be seen, the final model will produce calculations wherein $\bar{\theta}$ differs from θ_w because of nonlocal effects. In (18a), the sech function is quite small when $|\theta - \theta_w| = \pi/2$; nevertheless, the cutoff for $|\theta - \theta_w| > \pi/2$ improved the calculations in section 7 relative to data for small fetch.

S_{Tin} can be normalized in a number of ways—by $\sigma_p E_T$ or by various combinations of c_p or u_{*w} . After normalization by $c_p u_{*w}^2$, Terray et al. (1996) integrated $B(\sigma, \theta)E(\sigma, \theta)$ over frequency and angle; they also used (17) but used observed spectra in place of (9); our results (not shown) are very similar to theirs when similarly normalized.

Normalizing by u_{*w}^3 , S_{Tin}/u_{*w}^3 versus $\sigma_p U_{10}/g$ is plotted in Fig. 5a. This form is now familiar to modelers of ocean surface boundary layers. Noting that most of the wave energy source is directly dissipated into turbulence, values of $S_{Tin}/u_{*w}^3 = 100$ were empirically deduced by Craig and Banner (1994) and a value of 150 by Stacey (1999) as a source term in the turbulence energy equation component of their surface boundary layer model. These values are consistent with young inverse wave ages in Fig. 5a.

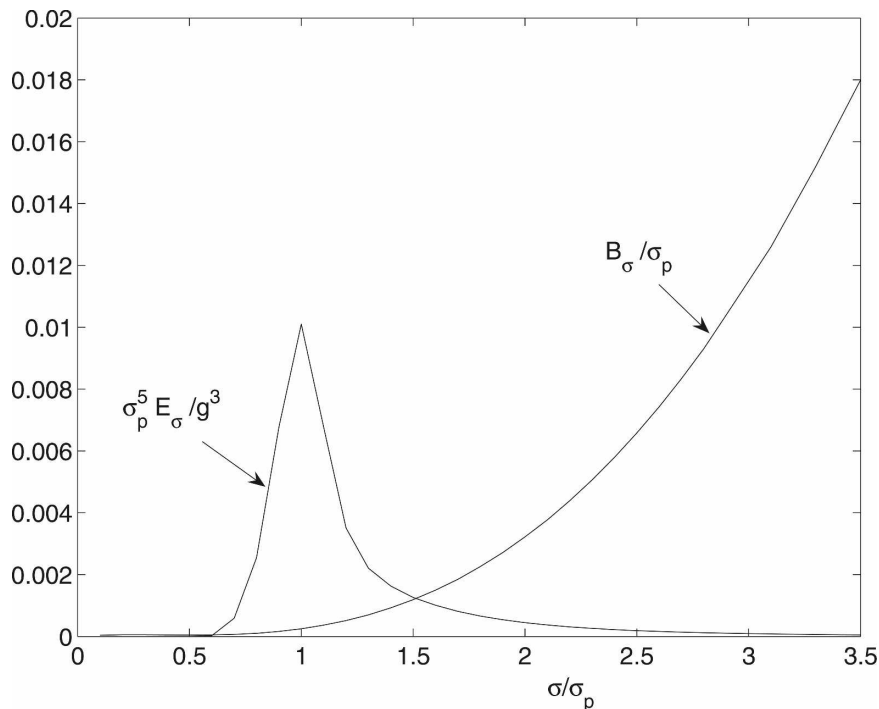


FIG. 3. A plot of the nondimensional DHH85 spectrum, Eq. (9), and the wave growth relation, Eq. (17), as a function of frequency for $U_{10}/c_p = \sigma_p U_{10}/g = 2.0$.

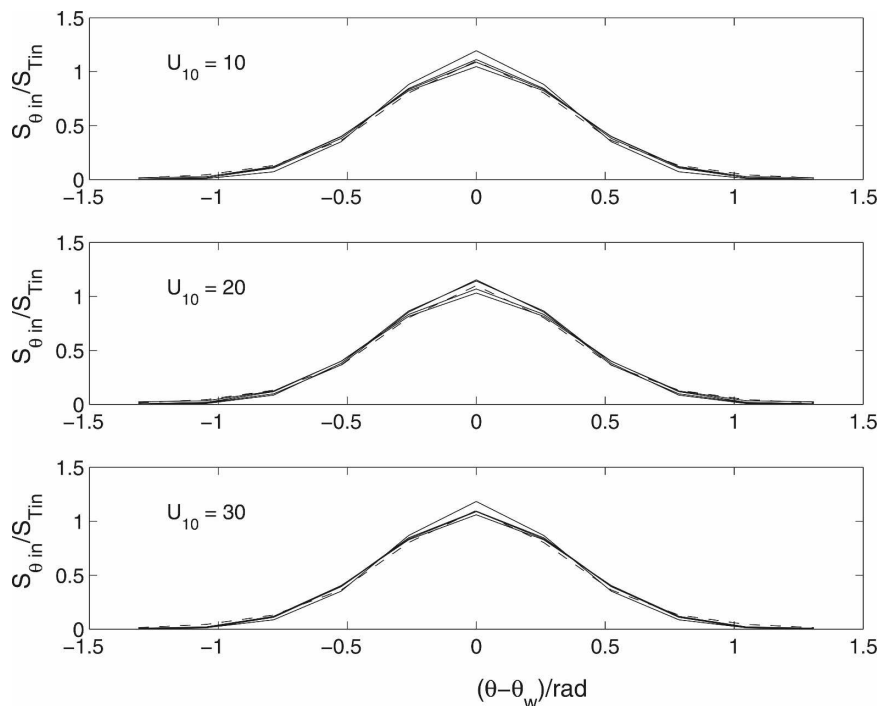


FIG. 4. The directional distribution of the wind energy source as functions of relative wave propagation angle, wind speed, and wave age (the closely packed curves with no labels): $U_{10} =$ (top) 10, (middle) 20, and (bottom) 30 m s^{-1} . The dependencies on wind speed and wave age are neglected in the model. The dependence on propagation angle is simply described by (18a) for $\beta = 2.2$, which is plotted as dashed curves.

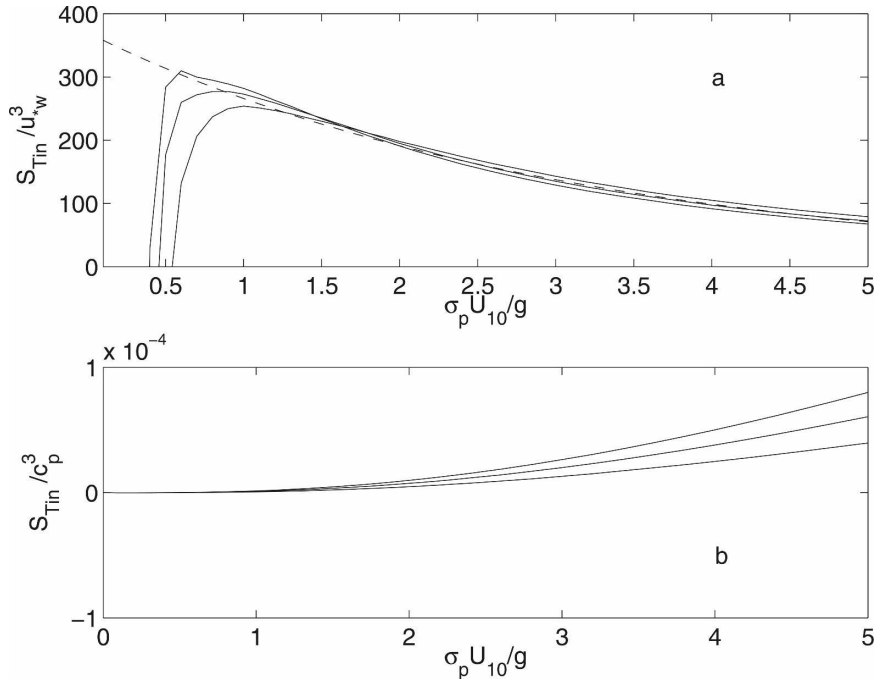


FIG. 5. The normalized wind energy source term as a function of wave age and wind speed (a) normalized on u_{*w}^3 ; dependence on wind speed is neglected; dashed line is from (18b) integrated over all angles and is used in the model; and (b) normalized on c_p^3 . The ascending curves are for $U_{10} = 10, 20,$ and 30 m s^{-1} , respectively. (The corresponding nondimensional parameter is $U_{10}[g(10 \text{ m})]^{-1/2} \cong 1, 2$ and 3 .)

The dashed line in Fig. 5a is given by $S_{\text{Tin}}/u_{*w}^3 = 370 \exp(-0.33\sigma_p U_{10}/g)$ but the calculated values abruptly decrease around $\sigma_p U_{10}/g = 0.5$ and become negative for lesser values. When S_{Tin}/c_p^3 is plotted versus $\sigma_p U_{10}/g$ as in Fig. 5b, the transition from positive to negative values is smooth. Furthermore, the negative values, occurring when the wave speed exceeds the wind speed as manifest in Eq. (17), are small and S_{Tin}/u_{*w}^3 is large only because u_{*w}^3 is very small. Thus, we let

$$S_{\theta\text{in}}/u_{*w}^3 = 370 \exp(-0.33U_{10}\sigma_p/g) f_{\text{spr}} \quad (18b)$$

In Fig. 5, S_{Tin}/u_{*w}^3 is, fortuitously, a weak function of U_{10} , whereas S_{Tin}/c_p^3 is dependent on U_{10} . Note that a fully developed wave field is often taken to be $U_{10}/c_p = \sigma_p U_{10}/g \cong 0.83$ and is considered to be an approximate number.

6. Wave dissipation

The total wave dissipation must be determined empirically. A model for white capping or wave breaking is

$$S_{\theta\text{Sdis}} = aS_{\theta\text{in}} + bE_{\theta}\sigma_p, \quad (19)$$

where a and b will be determined by reference to fetch data. The first term represents the fact that the high-frequency part of the spectrum is dissipated very nearly

in situ and the second part is dissipation of the mid- ($\sigma \approx \sigma_p$) to low-frequency part of the spectrum. This means, of course, that overall wave growth only responds to $(1 - a)S_{\theta\text{in}} - bE_{\theta}\sigma_p$; nevertheless, the full dissipation will be needed as input to the turbulence kinetic energy equation when this wave model is coupled to a circulation model. [To the second term in (19), we initially added a factor involving the wave slope but finding that results were insensitive to the addition, it was withdrawn.] An estimate of b as a function of a may be obtained by equating $S_{\theta\text{Sdis}} = S_{\theta\text{in}}$ for a fully developed sea when $\sigma_p U_{10}/g = 0.83$. Thus, dominant leverage on computed results are via the parameter, a , as determined in section 8.

There are many prescriptions for bottom frictional dissipation, generally for turbulent flow. There are uncertainties, but following the discussion in Booij et al. (1999) we adapt to the present model such that

$$S_{\theta\text{Bdis}}^{(1)} = C_b u_b^3 = C_b \frac{\sigma_{\theta}^3 (2E_{\theta}/g)^{3/2}}{\sinh^3 k_p D}, \quad (20a)$$

where u_b is the wave amplitude near the bottom. This formula agrees with that in Mellor (2002), where C_b is a function of nondimensional bottom roughness. Bottom roughness is generally unknown; here we suggest a

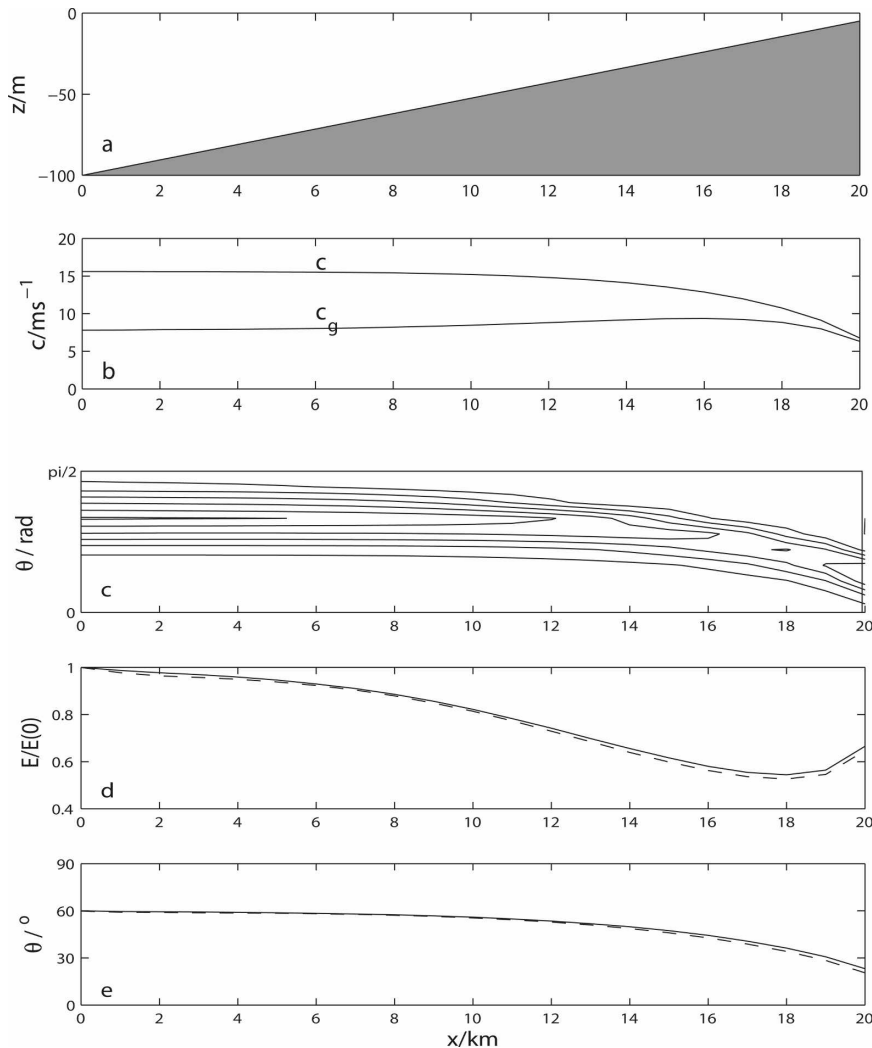


FIG. 6. A simple test of refraction wherein calculations from Eq. (8) are compared with Snell’s law for a wave period of 10 s. (a) The bottom topography. (b) The phase and group speed. (c) Contours of wave energy in propagation angle and distance space calculated from Eq. (8). (d) The angle integrated (total) wave energy per unit surface area calculated (solid line) and for constant energy flux (dashed line). (e) The mean wave propagation angle as calculated (solid line) and from Snell’s law (dashed line). The grid spacing is $\Delta x = 0.5$ km and $\Delta\theta = 15^\circ$.

typical value, $C_b = 0.003$. It should be noted that none of the suggested formulations in the wave modeling literature include the “streaming” effect described by Longuet-Higgins (1953).

The bottom can induce wave breaking if H_s/D is large enough. Following Battjes and Janssen 1978 [see appendix in Booij et al. (1999) for detailed discussion], we add to (20a) such that

$$S_{\theta Bdis}^{(2)} = \frac{E_\theta}{E_T} \frac{g\sigma_\theta}{8\pi} Q_b H_M^2, \quad (20b)$$

where the fraction of breaking waves out of an ensemble, Q_b , is given by the transcendental relation

$$(Q_b - 1) / \ln Q_b = 8(E_T/g)/H_M^2 \text{ and where } H_M = \gamma D; \text{ } \gamma \text{ is an empirically adjusted constant.}$$

Finally, $S_{\theta Bdis} = S_{\theta Bdis}^{(1)} + S_{\theta Bdis}^{(2)}$ for use in Eq. (8).

7. A directionally dependent frequency

A θ -dependent frequency is

$$\begin{aligned} \frac{\partial \sigma_\theta}{\partial t} + (\bar{c}_{g\alpha} + \bar{u}_{A\alpha}) \frac{\partial \sigma_\theta}{\partial x_\alpha} = & -\frac{\partial \sigma_\theta}{\partial k} \left(\frac{k_\alpha k_\beta}{k} \frac{\partial \bar{u}_{A\alpha}}{\partial x_\beta} \right) \\ & + \frac{\partial \sigma_\theta}{\partial D} \left(\frac{\partial D}{\partial t} + \bar{u}_{A\alpha} \frac{\partial D}{\partial x_\alpha} \right) + \Re, \end{aligned} \quad (21a)$$

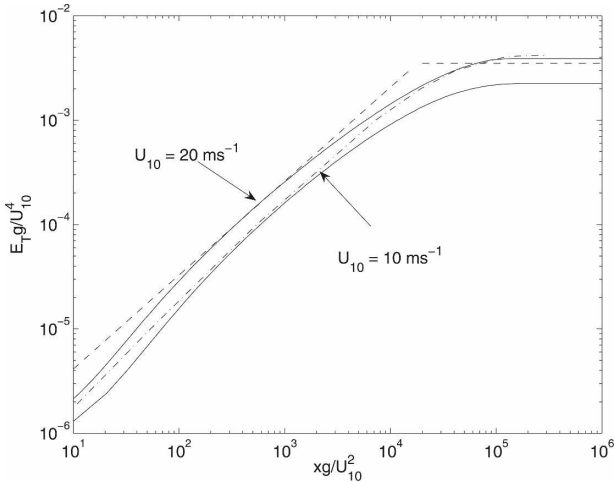


FIG. 7. The calculated fetch-dependent wave energy vs nondimensional fetch distance. Calculations for wind speeds, $U_{10} = 10$ and 20 m s^{-1} (solid lines), are compared with Eq. (23) (dashed line) and a result from Donelan et al. (1992) (dotted-dashed line). The later two curves represent a synthesis of observational data for a range of wind speeds. The wind angle is normal to the coast located at $x = 0$.

where $\partial\sigma_\theta/\partial k = \bar{c}_g$ and $\partial\sigma_\theta/\partial D = (\sigma_\theta/D)(n - 1/2)$. Equation (21a) is derived from wavenumber irrotationality, $\partial k_\alpha/\partial x_\beta - \partial k_\beta/\partial x_\alpha = 0$, and the conservation of crests, $\partial k_\alpha/\partial t + \partial\omega/\partial x_\alpha = 0$. In regions of θ that are wind driven ($f_{\text{spr}} > 0$), the additional source term, \mathfrak{R} , prescribed by

$$\mathfrak{R} = \sigma_p(\sigma_p - \sigma_\theta)f_{\text{spr}}^{1/2} \quad (21b)$$

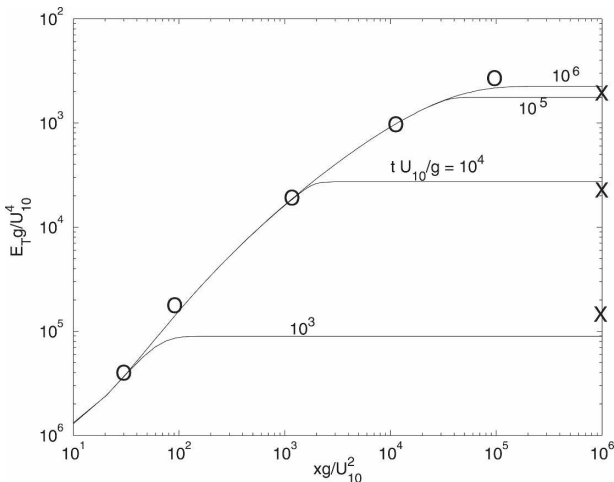


FIG. 8. The calculated fetch-dependent wave energy vs nondimensional fetch distance and duration for $U_{10} = 10 \text{ m s}^{-1}$. For $U_{10} = 20 \text{ m s}^{-1}$, the calculated values would be offset vertically as in Fig. 7. The “O”s are fetch-limited estimates from Hwang and Wang (2004, their Fig. 5). The “X”s are duration-limited estimates from the same source. See their paper for data scatter, which is greatest for large values of nondimensional x and t .

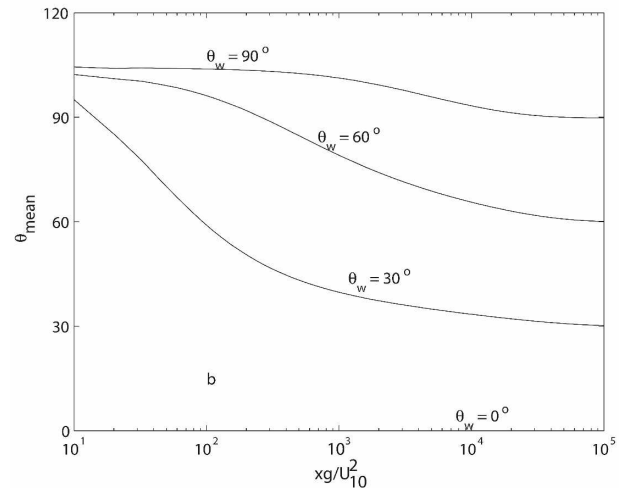
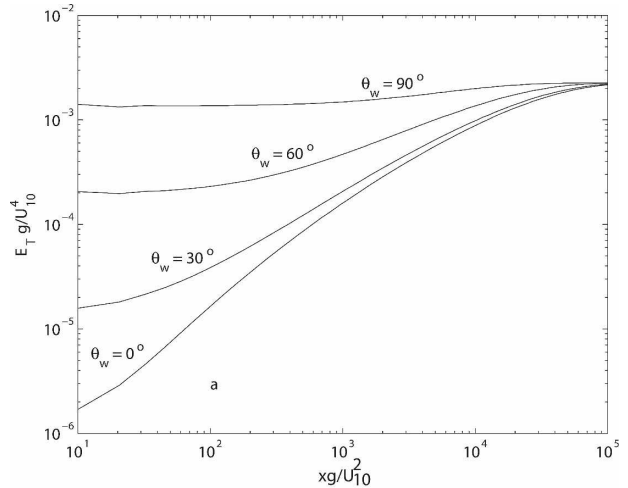


FIG. 9. (a) The same as in Fig. 7, but for a wind speed of $U_{10} = 10 \text{ m s}^{-1}$ and for different mean wind angles relative to the normal to the coast at $x = 0$. (b) A plot of the mean wave propagation angle, defined by Eq. (24), vs fetch.

has the effect of “nudging” (a term used, e.g., in data assimilation of various ocean properties) σ_θ toward σ_p .

8. Model tests

The model described above and whose independent variables are x , y , t , and θ was finite differenced and coded in FORTRAN replacing x , y , and θ by i , j , and m . Numerical details are in appendix B.

All of the tests in this section are independent of the coordinate, y . This was implemented by using only five rows in the j direction and setting cyclic boundary conditions on the bounding j cells. Alternately, a version of the code was created by stripping out the j terms. As a check on the code, the two versions gave the same results.

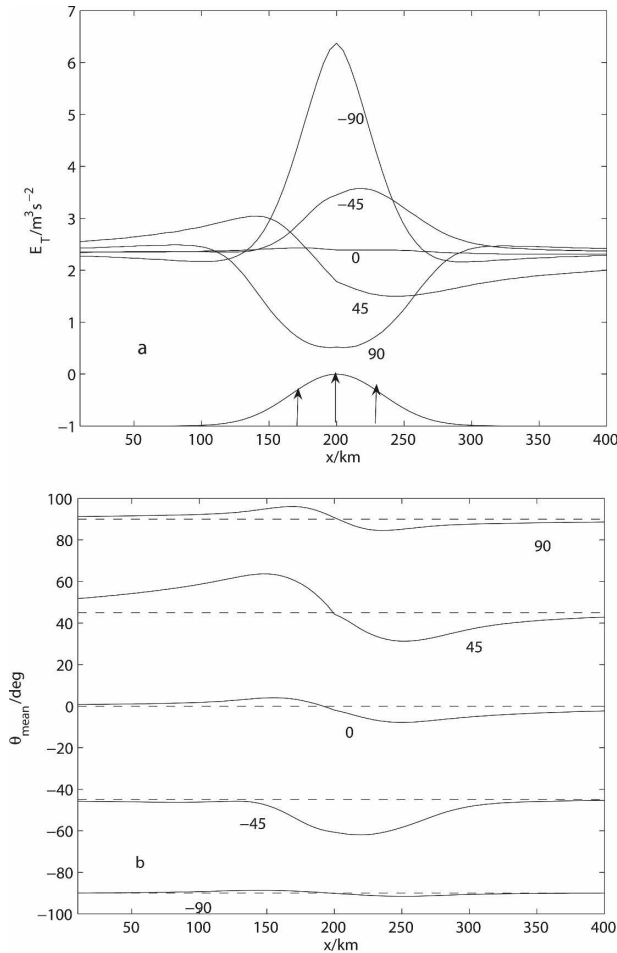


FIG. 10. The influence of a northward Gulf Stream-like jet (maximum velocity = 2 m s^{-1}) on waves forced by 10 m s^{-1} winds whose angle varies from 90° (northward; wind and jet velocities in the same direction) to -90° (southward; wind and jet velocities in opposite directions). (a) The variation of wave energy. The dashed line is the background fully developed wave field in the absence of the jet. (b) The variation of the mean propagation angle for the same wind angles as in (a).

a. Refraction for a monochromatic wave train

We first test the model against Snell's Law for the case $U_\alpha = 0$ and $U_{10} = 0$. At $x = 0$, incoming swell is prescribed according to $E_\theta \propto (\beta/2) \text{sech}^2[\beta(\theta - \theta_0)]$, where $\theta_0 = 60^\circ$ and $\beta = 4.0$, a rather narrow distribution with respect to θ . Equation (8) with a null right side is then solved to steady state. The time, spatial, and angle increments are 20 s, 500 m, and $2\pi/24 = 15^\circ$, respectively.

The bottom topography is shown in Fig. 6a. The frequency is $\sigma = \sigma_p = 2\pi/10\text{s}$, which according to (21) and conservation of crests, is constant; the corresponding $c(x)$ and $c_g(x)$ are plotted in Fig. 6b. The solution to Eq.

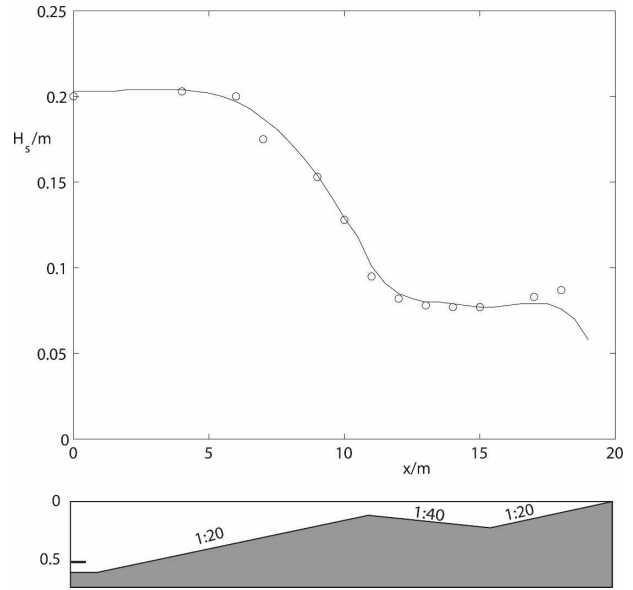


FIG. 11. Utilization of the depth-induced wave breaking formula, Eq. (20b) of Battjes and Janssen (1978), in (a) a calculation of wave breaking over (b) a shoaling bar. Data from the same authors.

(8) is given in Fig. 6c. Note that the angle domain is $-\pi < \theta < \pi$ but only the active portion is shown. In Fig. 6d, the total wave energy per unit surface area $E_T = \sum_{k=1}^{2\pi/\Delta\theta} E_\theta(\theta_k)\Delta\theta$, and is normalized with its value at $x = 0$. The mean angle, $\bar{\theta} = \sum_{k=1}^{2\pi/\Delta\theta} \theta E_\theta(\theta_k)\Delta\theta/E$, is shown in Fig. 6e.

Calculations are obtained from Snell's law so that

$$\theta(x, m) = \sin^{-1}[c(x) \sin\theta(0, m)/c(0)], \quad (22a)$$

$$E(x, m) = c_g(0) \cos\theta(0, m)E(0, m)/[c_g(x) \cos\theta(x, m)], \quad (22b)$$

and m is the label on each ray emanating from $x = 0$ where the initial distribution is as stated above. Averages are obtained on m and are plotted as the dashed lines in Figs. 6d,e. Agreement between the model and Snell's law is improved further (the two curves are nearly indistinguishable) by decreasing the angle increment from 15° to 10° .

b. Fetch-limited waves

The model was tested against the growth of waves for a constant offshore wind normal to a straight north-south coast located at $x = 0$. For this problem, similarity growth relations were formulated by Kitaigorodskii (1962) using dimensional analysis. As reported in Komen et al. (1994, p. 181), Kahma and Calkoen examined data from the JONSWAP experiment and data observed in the Bothnian Sea and Lake Ontario

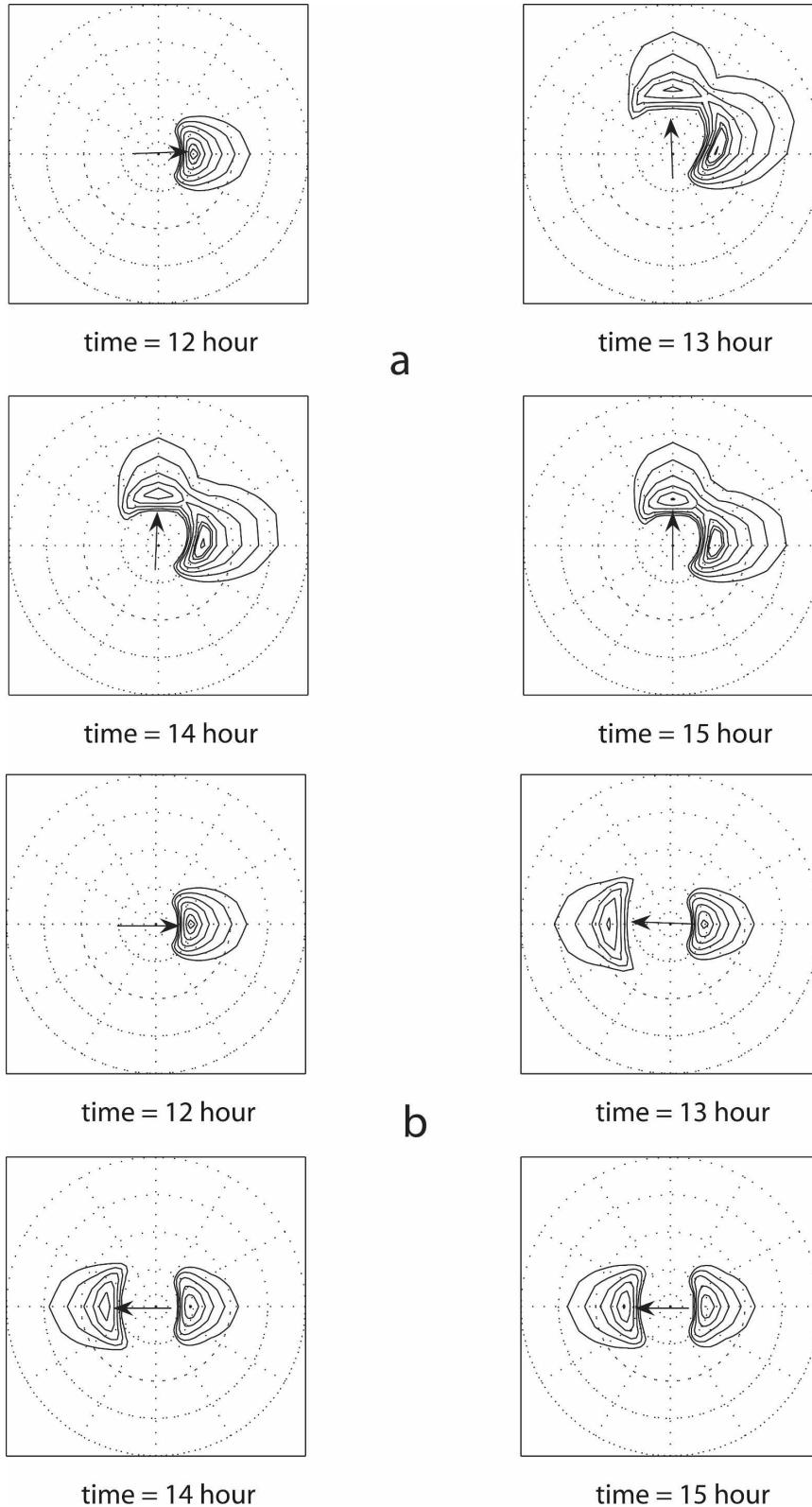


FIG. 12. Directional pseudospectra for a sudden change of wind direction for times of 12–15 h. The contours progressively increase by the factor 2. The dashed outer circle is for a maximum frequency $f_p = (2\pi)^{-1}\sigma_p = 0.4$ Hz; the contour interval is 0.1 Hz. (a) A homogeneous steady wind of 20 m s^{-1} is applied for 12 h starting from rest after which the direction is changed by 90° . The significant wave heights are successively 5.16, 5.45, 5.76, and 6.02 m. (b) The wind direction is changed by 180° . The significant wave heights are successively 5.16, 5.23, 5.31, and 5.39 m.

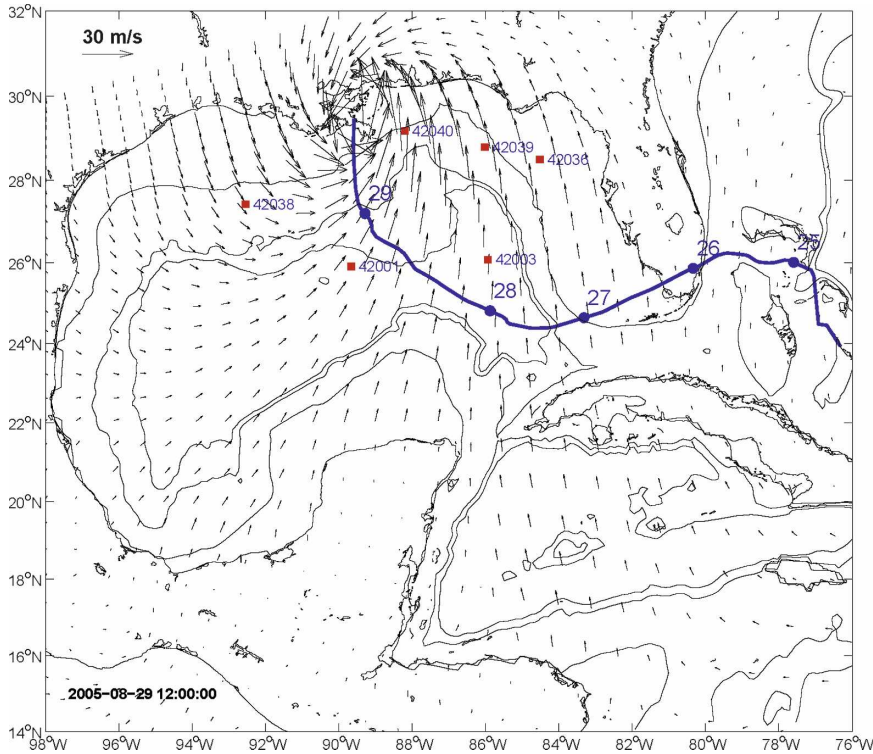


FIG. 13. The Gulf of Mexico. The path of Hurricane Katrina and the location of six NDBC buoys denoted by solid squares. The arrows are the 10-m wind vectors at 12 noon on 29 Aug 2005.

(DHH85). They first separated data into winds when the vertical density stratifications were stable or unstable. However, we deal only with the composite dataset that they represented by

$$\frac{E_T g}{U_{10}^4} = 5.4 \times 10^{-7} \left(\frac{xg}{U_{10}^2} \right)^{0.9} \quad (23)$$

and that is plotted as a dashed line in Fig. 7. The well-developed limit of $E_T g / U_{10}^4 = 3.6 \times 10^{-3}$ is from Pierson and Moskowitz (1964).

Another fit to Lake St. Clair data by Donelan et al. (1992), using an elaborate analysis scheme to minimize inhomogeneities in the data, is shown as a dotted-dashed line in Fig. 7.

The solid lines are from the present model for two different values of U_{10} and for the best-fit parameters, $a = 0.925$, $b = 0.18 \times 10^{-4}$; these values are hereafter held constant except for swell portions of E_θ ($f_{spr} < 0$) as described below, where b is reduced by a factor of 5. The time and angle increments are 10 s and 15° respectively; at $x = 0$, the spatial step is $\Delta x = 100$ m but thereafter $\Delta x(i + 1) = 1.10\Delta x(i)$.

Whereas the data syntheses exclude dependence

on U_{10} , there must be some model dependence on U_{10} or, in dimensionless form, $U_{10}[g(10\text{ m})]^{-1/2}$ according to dimensional analysis or from (15a)–(15c), (16), and (17) together with the relation $H_S = 4(E/g)^{1/2}$.

In Fig. 8 we show calculations of the time and distance development of wave growth together with a synthesis of data by Hwang and Wang (2004). Since duration-limited data are scarce and difficult to obtain, they deduced duration-limited growth from fetch-limited growth and compared with their own and other datasets; a synthesis of their duration-limited data is also shown in Fig. 8. A comparison (not shown) of non-dimensional peak frequency $\sigma_p U_{10}/g$ versus xg/U_{10}^2 was also quite favorable.

Figures 9a,b demonstrate the fetch-limited behavior for $U_{10} = 10$ m and for different wind angles relative to the eastward direction; the coastline is north–south at $x = 0$. For wind angles not equal to zero and, because of the spread of the wind growth term in (18) denoted by f_{spr} , waves with mean propagation angles larger than the wind angle will propagate over a longer fetch and therefore accrue higher energies than waves with lower angles; the mean wave angle therefore differs from the wind angle until a considerable distance from the coast

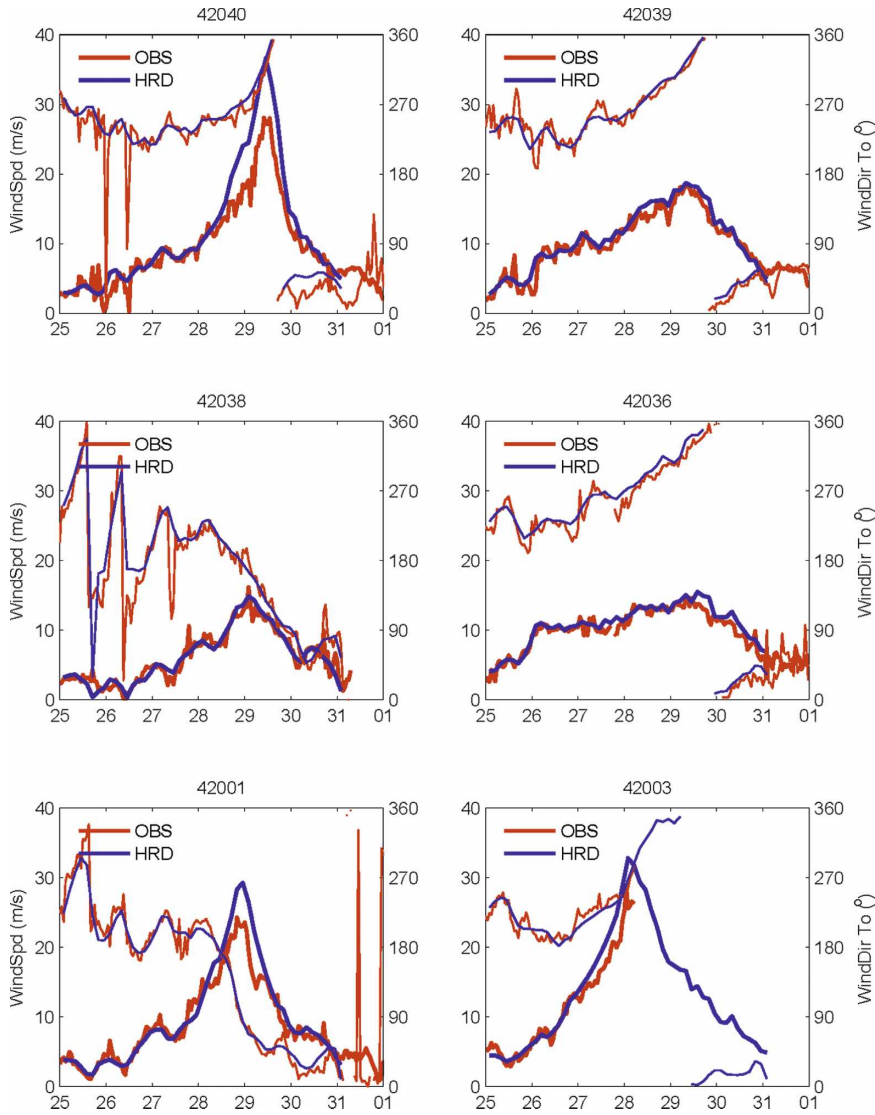


FIG. 14. The analyzed (blue lines) wind speeds and directions (measured from true north; e.g., 90° for wind toward the east) from the NOAA HRD of AOML compared to the data (red lines) obtained by the six NDBC buoys. All winds are referenced to the 10-m height.

where the two angles coincide. The mean wave angle is given by

$$\bar{\theta} = \tan^{-1} \left(\frac{\int_{-\pi}^{\pi} E_{\theta} \sin \theta \, d\theta}{\int_{-\pi}^{\pi} E_{\theta} \cos \theta \, d\theta} \right). \tag{24}$$

For small wind angles, say $\theta_w = \pi/6 = 30^\circ$ at the coast ($x = 0$), energy input near the wind angle is small since the effective fetch is small and the flow angle is dominated by wave propagation components around $\theta = 90^\circ$ corresponding to very large fetch. Consider the

extreme case of wind parallel to the coast, $\theta_w = \pi/2 = 90^\circ$. At the coast, the wind only produces waves in the range $0 < \theta < \pi/2$ whereas, in the far field ($x \rightarrow \text{large}$), the wind produced the full range $0 < \theta < \pi$; thus the mean wind angle is larger and the energy smaller at the coast than the far field. Relatively, energy propagating from the far field to the coast has dissipated before reaching the coast.

c. Refraction due to currents

A northward Gulf Stream–like jet is prescribed according to

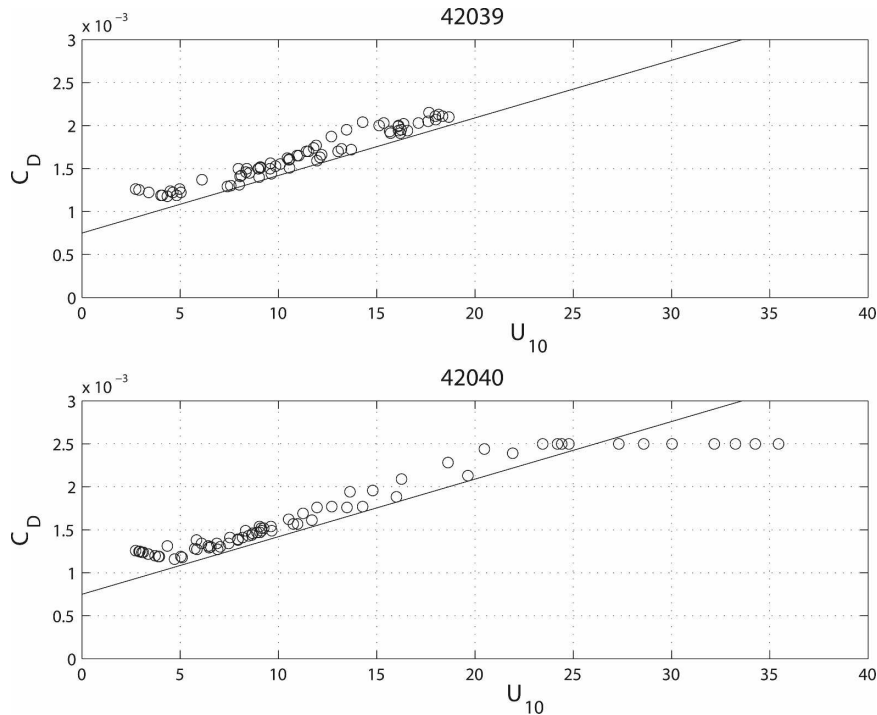


FIG. 15. Model-calculated C_D as a function of the 10-m wind speed for two of the buoys: (top) 42039 for which C_D was not limited to the value 0.0025, and (bottom) 42040 for which wind speeds were greater and C_D was limited. The straight line, after Garratt (1977), is $C_D = (0.75 + 0.067U_{10})10^{-3}$.

$$V = 2.0 \text{ m s}^{-1} \exp\left[\left(\frac{x - L/2}{50 \text{ km}}\right)^2\right] \exp\left(\frac{z}{1000 \text{ m}}\right), \quad (25)$$

where $L = 400 \text{ km}$ is the domain zonal width. The spatial, temporal, and angle increments are 5 km , 500 s , and 15° , respectively. Since the waves are confined to the near surface, the depth dependence is not important in this application, but the code generally does account for depth dependence through the interaction terms in (8).

A background, fully developed wave field is first established in the absence of the jet with a wind speed of $U_{10} = 10 \text{ m s}^{-1}$ and varying directions, northward (90°) through southward (-90°); wave energy and the mean propagation angle are shown in Fig. 10 as dashed lines. Here, lateral boundary conditions are devised so that fully developed wave energy propagates through the domain boundaries. The mean propagation angles are the same as the wind direction.

With the jet in place, the solid curves in Fig. 10 show the deviations of wave energy and mean angle. Analysis of the calculations show that, in this application, the term $(k_\alpha/k) \sin\theta \partial \bar{u}_{A\alpha}/\partial x = \sin^2\theta \partial V/\partial x$ in (13a) is mostly responsible for the current-induced deviations.

However, the fact that the friction velocity in (15a) depends on the wind speed relative to the surface water speed has some effect; for example, in the -90° case (opposing wind and jet), the enhanced friction velocity—and therefore enhanced $S_{\theta m}$ —accounts for 15% of the total increase at $x = 200 \text{ km}$.

It is noted that wave models that recognize only depth-averaged currents would produce smaller deviations by the factor 4, say, for a depth of 4000 m .

d. Depth-induced wave breaking

The model is next applied to the depth-induced wave breaking experiment of Battjes and Janssen (1978), which invokes the dissipation relation, (20b), by the same authors. Waves are produced upstream by a wavemaker and propagate into the measurement region. The frequency is 0.53 Hz and the upstream boundary condition is $E_\theta = (.025 \text{ m}^3 \text{ s}^{-2})(\beta/2) \text{ sech}^2(\beta\theta)$ for $\beta = 2.2$. The bottom friction term (20a) is a negligible addition to $S_{\theta Bdis}$ in this case. Figure 11 shows the significant wave height distribution for $\gamma = 0.70$, a best-fit value close to that chosen by Booij et al. (1999) for their third-generation model comparison with the same experiment. Their result and that in Fig. 11 shows that (20b) is a remarkable relation even

though it includes an adjustable constant. By examining field data, Ruessink et al. (2003) propose a dependency on kh such that $\gamma = 0.76kh + 0.29$.

Since the wave breaking-induced current and setup may have some influence, this calculation should be repeated when the wave model is coupled with a circulation model.

e. Sudden change in wind direction and swell

Figure 12a demonstrates the response of directional spectra to a sudden 90° change in a 20 m s^{-1} , homogeneous wind field after a 12-h spinup from rest. One can, if one wishes, label Fig. 12a directional pseudospectrum since the frequency distribution is parameterized using (9) consistent with the calculated values of E_θ . The portion that is wind driven is delineated by $f_{\text{spr}} > 0.0$ and the dissipation constant, as before, is $b = 0.18 \times 10^{-4}$; otherwise, the dissipation constant is reduced by a factor of 5, to the value $b = 0.036 \times 10^{-4}$. This result may be compared with a similar case using the third-generation model of Tolman (1991) and Tolman and Chalikov (1996). Their results are understandably more diffuse, but similarly attenuate the higher-frequency energy of the swell component compared to the present result. The swell decay rate constant is uncertain; the value, 0.036×10^{-4} , corresponds to decay by e^{-1} in about 6 days and is an estimate—with help from a spatial to temporal transformation—from Snodgrass et al. (1966) for swell dissipation not far from the source. Having introduced the possibility of swell in the model, we now note that $E_{\text{TW}} = \int E_\theta d\theta$ where the integration is limited by the region where $f_{\text{spr}} > 0$.

Figure 12b is a case wherein the wind direction changes by 180° . Compared to the eastern portion of Fig. 12a, the swell component in the eastern portion of Fig. 12b decays faster since the winds experience a negative S_{oin} . This is accomplished by simple addition of a negative mirror image to f_{spr} in (18a) but multiplied by the factor 0.4 as suggested by the laboratory experiments of Donelan (1999), which demonstrated a rapid wave decay if opposed to the wind direction. Arduhin et al. (2007) suggest that this factor is too high compared to field data; however, this is based on data where wind and wave directions are significantly not colinear in which case $f_{\text{spr}} < 1$.

9. Hurricane Katrina

During the period 25–30 August 2005, Hurricane Katrina swept through the Florida Strait and into the Gulf of Mexico with a devastating landfall in and around

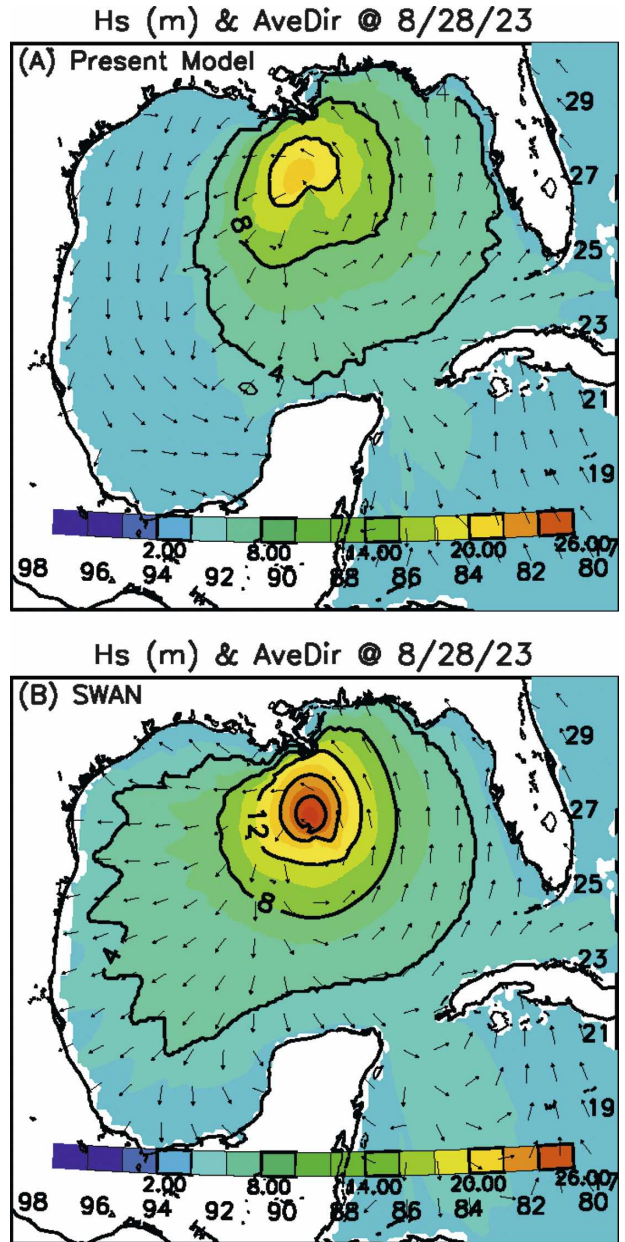


FIG. 16. A comparison of wave direction given by arrows and significant wave height (contours) calculated by the (a) present model and (b) SWAN on the 23rd hour of 28 Aug 2005. If the limit on C_D is removed from the present model, the peak significant wave heights of both models are in agreement.

New Orleans during the period. The path of the hurricane is shown in Fig. 13. There were six National Data Buoy Center (<http://www.ndbc.noaa.gov/>) buoys in the neighborhood of Katrina’s path; they are located in Fig. 13.

Yin and Oey (2007) have applied POM to the Gulf of Mexico forced by winds analyzed and obtained from the National Oceanic and Atmospheric Administration

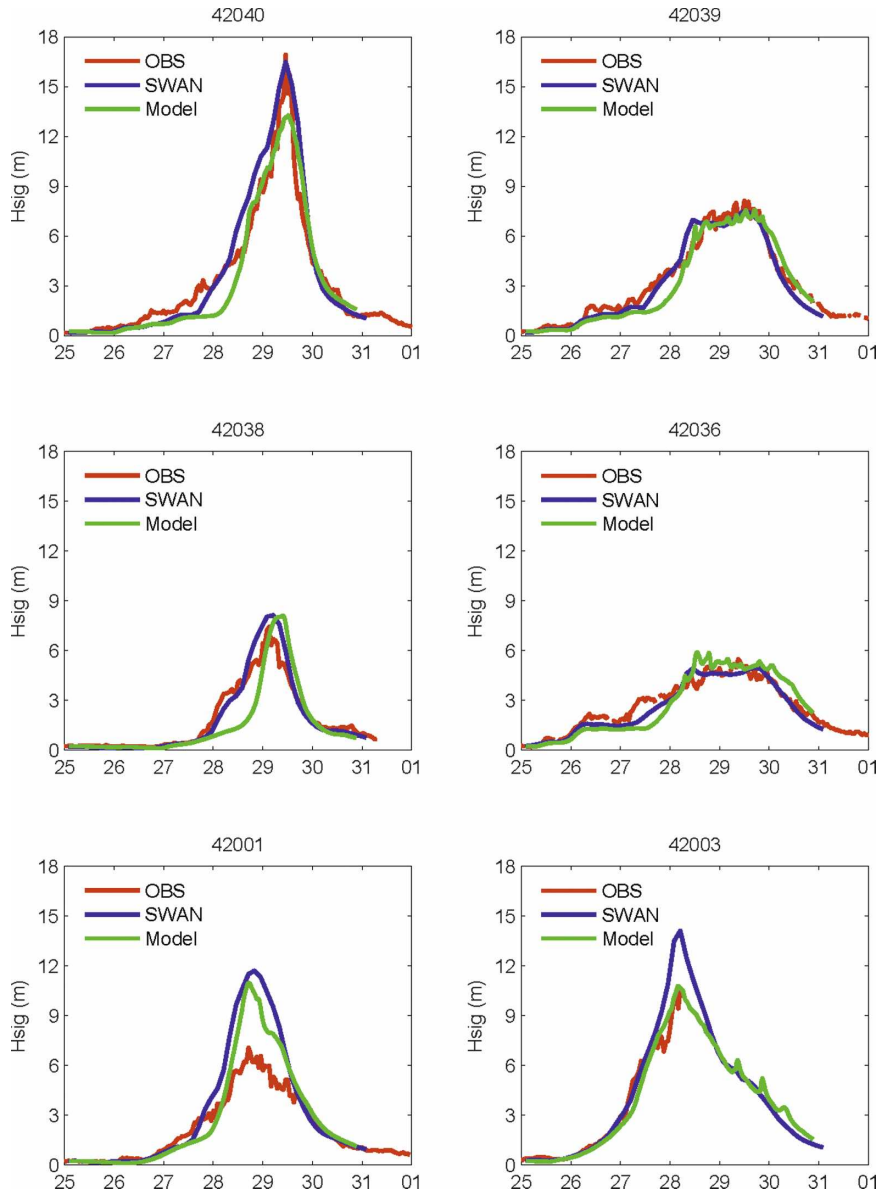


FIG. 17. For the six buoys, significant wave heights from the buoy data (red lines) and as calculated by SWAN (blue lines) and the present model (green lines).

(NOAA) Hurricane Research Division (HRD) of the Atlantic Oceanographic and Meteorological Laboratory (AOML; available online at <http://www.aoml.noaa.gov/hrd/>). The wind speed—referenced to 10-m height—and direction are shown in Fig. 14 and are compared with the winds obtained by the buoys. We use these winds only to force the wave model. In keeping with the purpose of this paper (slightly violated in Gulf Stream-like jet case above) to establish the wave model cum sole prior to coupling with a general circulation model, current interactions are neglected. This will also enable a direct comparison with results using the SWAN model.

To accommodate large wind velocities, drag coefficients are limited to the value $C_D = C_{Dmax} = .0025$, applicable to winds over 25 m s^{-1} (and therefore not a factor in our previous calculations); this flattening of the drag coefficient curve is a relatively recent finding by Powell et al. (2003), Donelan et al. (2004), and Emanuel (1995, 2003). Reasons advanced by these authors for the flattening include high concentration of water droplets (spume) near the surface or high curvature of wave forms such that the airflow “skips” from crest to crest and pressure in the trough is relatively constant. At three of the buoys (42040, 42001, and 42003), the model-derived $C_D(U_{10})$ from

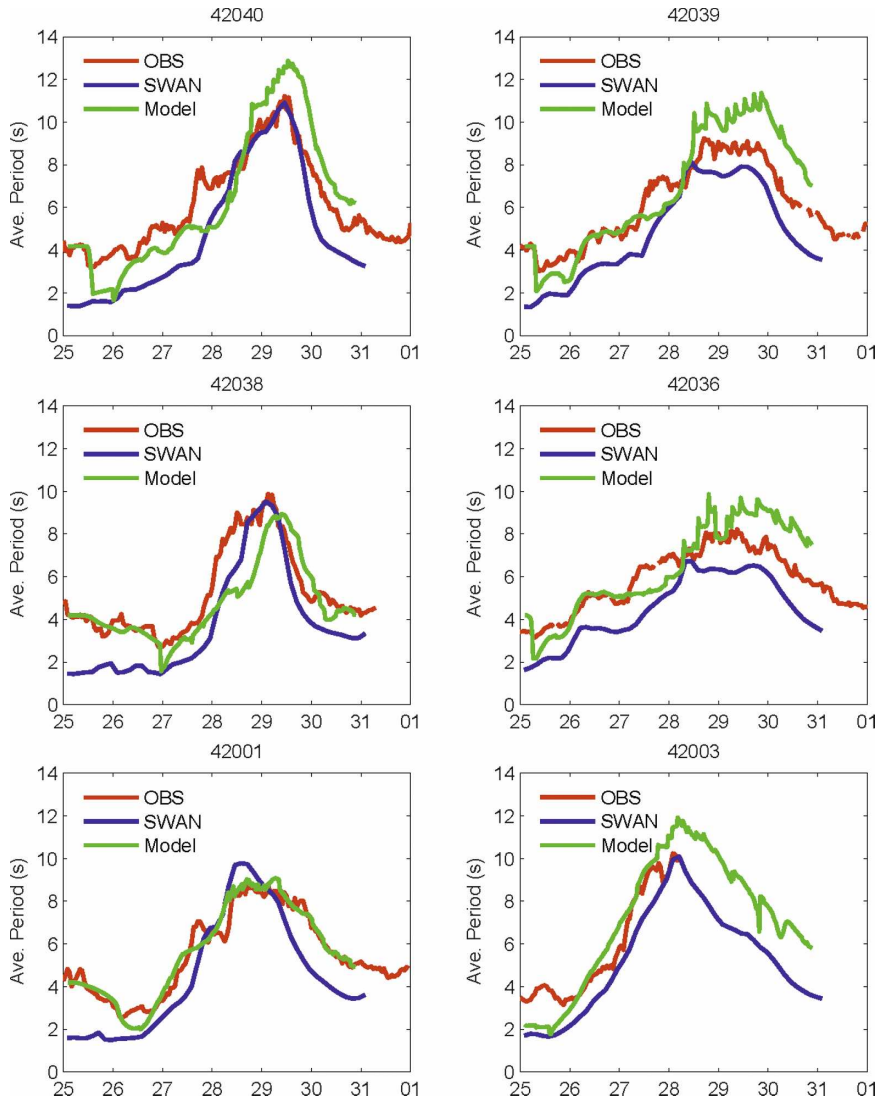


FIG. 18. For the six buoys, average wave periods from the buoy data (red lines) and as calculated by SWAN (blue lines) and the present wave model (green lines).

(15b) and (15c) exceeded C_{Dmax} at the wind speed of 25 m s^{-1} ; the other three buoys (42039, 42036, and 42038) did not exceed this limit; Fig. 15 illustrates $C_D(U_{10})$ for a case wherein C_D was not limited and a case wherein the limits were invoked. It should be noted that calculated inverse wave ages (not shown) were confined to the range $0.7 < \sigma_p U_{10}/g < 1.8$ so that most of the variation of $C_D(U_{10})$ as given by (15b) and (15c) depends on H_S , which is approximately proportional to U_{10}^2 .

Figure 16 is a plan view of the model output of significant wave height, and wave propagation direction from the present model and from SWAN on the 23rd hour of 28 August 2005. The peak value for SWAN was 22 m and for the present model 15 m. The C_D limit was

not applied to the SWAN calculations and, if the limit on C_D is removed, the present peak significant wave height is also 22 m.

Figure 17 shows comparisons of significant wave height calculated by the present model, SWAN, and the buoy data. For buoy 42038, SWAN anticipates the arrival of swell better than the present model; for buoy 42001, both have overly large maximum H_S , SWAN somewhat more so than the present model. The present model seems to simulate the maximum H_S better for buoy 42003, but this buoy capsized at the time when both models indicate the arrival of the peak. The present model somewhat underestimates the maximum H_S for buoy 42040.

The average wave period, $T_{ave} \equiv E_T(\int_{-\pi}^{\pi} \sigma_{\theta} E_{\theta} d\theta)^{-1}$,

is shown in Fig. 18. For buoy 42001, the error calculated by the present model is quite small; otherwise, errors on the order of 1–2 s are incurred by both models.

10. Summary

A surface gravity wave model has been developed; it includes depth-dependent wave–current interaction terms in both the wave energy equation and the ocean circulation equations derived in (the revised) M03. Except for section 9, the model is presented as a stand-alone model but it is designed so that coupling with three-dimensional circulation models is possible in operational or climate applications. The stand-alone wave model comprises Eqs. (8), (11), (12b), (13), (15), (18), (19), (20), and (21) and the conditions that, if $f_{spr}(\theta) \geq 0.0$, $b(\theta) = 0.18 \times 10^{-4}$; otherwise, $b(\theta) = 0.036 \times 10^{-4}$.

Model calculations compare favorably with established fetch and duration “laws.” Other applications were presented to demonstrate model versatility. Hurricane Katrina model–data comparisons, which contained low to high wind forcing, demonstrated significant model generality. This simple and computationally economic model produced wave properties comparable to buoy data and comparable to those obtained with the third-generation model SWAN.

The next step will be to compare a fully coupled circulation and wave model with laboratory and field data. The wave model will then include currents in (8). The circulation model’s momentum equation will include wave parameters in the wind stress relation, incorporation of depth-dependent radiation stress terms, and incorporation of wind–wave-induced pressure momentum transfer into the water column. The model’s turbulence kinetic energy equation will include a source term equal to wave dissipation. It is to be expected that wave–ocean coupling will reduce the errors discussed above, but ultimately predictive modeling of the general circulation of either fluid will require fully coupled atmosphere–wave–ocean models.

Acknowledgments. Some of this research was conducted while GLM was a visiting professor at the Technical University of Delft; he is indebted to the faculty and staff of the Fluid Mechanics Section for valuable consultation. GLM was supported by the NOPP surf-zone project, by ONR Grant N0014-01-1-0170, and partially by DOI/MMS Contract 1435-01-03-CT-72021. GLM and MAD are presently funded by NSF OCE0526508 and OCE0526491. LYO was supported by MMS Contract 1435-01-06-CT-39731.

APPENDIX A

Spectral Averages

The functions used in section 4 are defined by

$$F_{c\theta}(k_p D) = E_T^{-1} \int_0^\infty E_\sigma \frac{c_\theta}{c_p} \left(\frac{\cosh k_p D}{\cosh k D} \right)^2 d\sigma, \quad (A1)$$

$$F_1(k_p D, \varsigma) = E_T^{-1} \int_0^\infty E_\sigma(k/k_p) F_{CS} F_{CC} d\sigma, \quad (A2)$$

$$F_2 = E_T^{-1} \int_0^\infty E_\sigma(k/k_p) F_{SC} F_{SS} d\sigma, \quad (A3)$$

$$F_3 = E_T^{-1} \int E_\sigma k D [(F_{CS} F_{CC} + F_{SS} F_{SC})/2 + F_{CS} F_{SS}] d\sigma. \quad (A4)$$

The behavior of the various functions is useful to check the numerical calculations and to extend the numerical results for large and small $k_p D$. First, the monochromatic functions behave as follows:

$k_p D \rightarrow$	0	∞
F_{SS}	$1 + \varsigma$	$\exp(kD\varsigma)$
F_{CS}	$1/kD$	$\exp(kD\varsigma)$
F_{CC}	1	$\exp(kD\varsigma)$
F_{SC}	0	$\exp(kD\varsigma)$

The behavior of the spectrally averaged functions obtained by numerical integration is as follows:

$k_p D \rightarrow$	0	∞
F_1	$1/K_p D$	$1.83 \exp(5.41 k_p D \varsigma)$
F_2	0	F_1
F_3	$3/2 + \varsigma$	$3.66 k_p D \exp(6.14 k_p D \varsigma)$

The constants in $F_1(k_p D \rightarrow \infty) = F_2(k_p D \rightarrow \infty)$ are obtained from a fit to the calculations at the two top-most points, $\varsigma = -0.0$ and -0.05 . For monochromatic waves, we would simply have $\exp(2kD\varsigma)$. A lookup table was prepared using numerical integrations for $k_p D = 0.2, 0.4, \cdot, \cdot, \cdot, 3.0, 100.0$.

For $k_p D \geq 3.0$, all of the functions in (5) revert to simple exponentials dependent on $k_p D$ and $k_p z$. The result is that $F_1(k_p D, k_p z) = F_1(100, k_p z)$ and $F_3(k_p D, k_p z) = (k_p D/100) F_3(100, k_p z)$. These rules are verified by the numerical integrations for $k_p D = 3.0$.

APPENDIX B

Some Numerical Details

The following code will accommodate an orthogonal curvilinear grid in x, y space in the sense of a finite volume. The leapfrog tendency term is split so that

$$\Delta x \Delta y \frac{\tilde{e}_{i,j,m} - e_{i,j,m}^{n-1}}{2\Delta t} + F_{X,i+1,j,m}^n - F_{X,i,j,m}^n + F_{Y,i,j+1,m}^n - F_{Y,i,j,m}^n = 0, \quad (B1)$$

where

$$F_{X,i,j,m}^n = [0.5c_{gx,i,j,m}(e_{i,j,m}^n + e_{i-1,j,m}^n) - \gamma|c_{gx,i,j,m}|(e_{i,j,m}^{n-1} - e_{i-1,j,m}^{n-1})]\overline{\Delta y}, \quad (B2a)$$

$$F_{Y,i,j,m}^n = [0.5c_{gy,i,j,m}(e_{i,j,m}^n + e_{i,j-1,m}^n) - \gamma|c_{gy,i,j,m}|(e_{i,j,m}^{n-1} - e_{i,j-1,m}^{n-1})]\overline{\Delta x}. \quad (B2b)$$

The orthogonal cell dimensions are Δx and Δy reckoned at the cell center; they may vary from cell to cell according to a particular curvilinear grid. The group velocity components and $\overline{\Delta x}$ and $\overline{\Delta y}$ are located at the edge of each cell. After executing (B1), $\tilde{e}_{i,j,m} = \max(\tilde{e}_{i,j,m}, 1 \times 10^{-5})$; the lower limit corresponds to $H_S = 1$ mm.

The terms modified by the γ coefficient are diffusion-like terms. For $\gamma = 0$, the result is pure central differencing, whereas for $\gamma = 0.5$, the result is pure upwind. Most calculations in the main text used $\gamma = 0.2$. However, at cells adjacent to boundaries we stipulate local upwinding by setting $\gamma = 0.5$. In general, the difference in calculated results between the two values of γ was quite small.

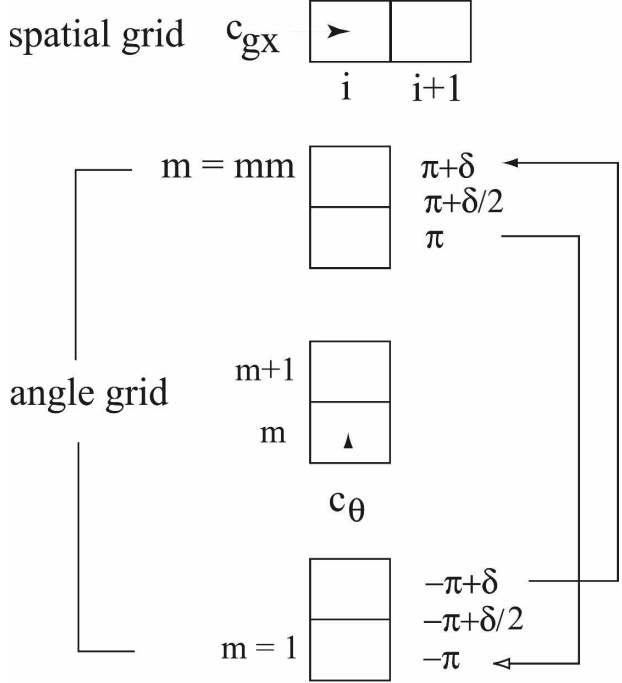
After (B1), the time step in angle space is

$$\frac{\hat{e}_{i,j,m} - \tilde{e}_{i,j,m}}{2\Delta t} + \frac{F_{\theta,i,j,m+1}^n - F_{\theta,i,j,m}^n}{\Delta\theta} = D, \quad (B3)$$

where

$$F_{\theta,i,j,m}^n = 0.5(c_{\theta,i,j,m} + |c_{\theta,i,j,m}|)e_{i,j,m-1}^n + 0.5(c_{\theta,i,j,m} - |c_{\theta,i,j,m}|)e_{i,j,m}^n. \quad (B4)$$

Initially $D = 0$ so that (B3) and (B4) combine for a pure upwind differencing and positive definite algorithm. However, following Smolarkiewicz (1984), the solution



$$mm = mseq+2$$

$$\delta = 2\pi/mseg$$

FIG. B1. The computational stencil emphasizing the propagation angle grid and the cyclic boundary conditions. Wave energy, $e_{i,j,m}$, is located at the center of each cell and the speeds, $c_{gx,i,j,m}$, $c_{gy,i,j,m}$, and $c_{\theta,i,j,m}$, are located at the edge of each cell.

is iterated such that an antidiffusion D is calculated to reduce the diffusion incurred by upwinding; it is inserted into (B3) for each iterant (three iterations are sufficient) while maintaining positive definiteness. For the details in calculating D , the reader is referred to the paper by Smolarkiewicz. A grid stencil, emphasizing the angle grid, is shown in Fig. B1. The angle space is $-\pi$ to $+\pi$. Cyclic boundary conditions connect the branch cut at $-\pi, \pi$.

Finally the source terms, (18) and (19), are included such that

$$\frac{e_{i,j,m}^{n+1} - \hat{e}_{i,j,m}}{2\Delta t} = A + Be_{i,j,m}^{n+1}, \quad (B-5)$$

so that the part of $S_{\theta in} + S_{\theta dis} = A + Be_{i,j,m}^{n+1}$ that is dependent on $e_{i,j,m}$ is executed implicitly.

The discretization for (21) is

$$\sigma_{i,j,m}^{n+1} - \sigma_{i,j,m}^{n-1} = \frac{\Delta t}{\Delta x} [-c_{gx,i,j,m}(\sigma_{i+1,j,m} - \sigma_{i-1,j,m}) + \gamma|c_{gx,i,j,m}|(\sigma_{i+1,j,m} - 2\sigma_{i,j,m} + \sigma_{i-1,j,m})] \quad (B-6)$$

plus similar terms for the y direction and terms for the right-hand side of (21a).

REFERENCES

- Alves, J. H. G. M., M. L. Banner, and I. R. Young, 2003: Revisiting the Pierson–Moskowitz asymptotic limits for fully developed wind waves. *J. Phys. Oceanogr.*, **33**, 1301–1323.
- Ardhuin, F., T. H. C. Herbers, G. P. van Vledder, K. P. Watts, R. Jensen, and H. C. Graber, 2007: Swell and slanting fetch effects on wind growth. *J. Phys. Oceanogr.*, **37**, 908–931.
- Banner, M. L., 1990: Equilibrium spectra of wind waves. *J. Phys. Oceanogr.*, **20**, 966–984.
- Battjes, J. A., and J. P. F. M. Janssen, 1978: Energy loss and set-up due to breaking of random waves. *Proc. 16th Int. Conf. of Coastal Engineering*, New York, NY, American Society of Civil Engineers, 569–587.
- Booij, N., R. C. Ris, and L. H. Holthuijsen, 1999: A third-generation wave model for coastal regions. 1. Model description and validation. *J. Geophys. Res.*, **104**, 7649–7666.
- Craig, P. D., and M. L. Banner, 1994: Modeling wave-enhanced turbulence in the ocean surface layer. *J. Phys. Oceanogr.*, **24**, 2546–2559.
- Donelan, M., M. Skafel, H. Graber, P. Liu, D. Schwab, and S. Venkates, 1992: On the growth of wind-generated waves. *Atmos.–Ocean*, **30**, 457–478.
- , 1977: A simple numerical model for wave and wind stress prediction. Nat. Water Res. Inst. Rep., Burlington, ON, Canada, 27 pp.
- , 1990: Air–sea interaction. *The Sea*, B. LeMehaute and D. M. Hanes, Eds., Ocean Engineering Science, Vol. 9, John Wiley and Sons, 239–292.
- , 1999: Wind-induced growth and attenuation of laboratory waves. *Wind-over-Wave Couplings*, S. G. Sajjadi, N. H. Thomas, and J. C. R. Hunt, Eds., Clarendon Press, 183–194.
- , J. Hamilton, and W. H. Hui, 1985: Directional spectra of wind-generated waves. *Philos. Trans. Roy. Soc. London*, **A315**, 509–562.
- , B. K. Haus, N. Reul, W. J. Plant, M. Stiassnie, H. C. Graber, O. B. Brown, and E. S. Saltzman, 2004: On the limiting aerodynamic roughness in very strong winds. *Geophys. Res. Lett.*, **31**, L18206, doi:10.1029/2004GL019460.
- Emmanuel, K., 1995: Sensitivity of tropical cyclones to surface exchange coefficients and a revised steady state model incorporating eye dynamics. *J. Atmos. Sci.*, **52**, 3969–3976.
- , 2003: A similarity hypothesis for air–sea exchange of extreme wind speeds. *J. Atmos. Sci.*, **60**, 1420–1428.
- Garratt, J. R., 1977: Review of drag coefficients over oceans and continents. *Mon. Wea. Rev.*, **105**, 915–929.
- Golding, B. W., 1978: A depth dependent wave model for operational forecasting. *Turbulent Fluxes through the Sea Surface, Wave Dynamics and Prediction*, A. Favre and K. Hasselmann, Eds., Plenum Press, 593–604.
- Hasselmann, K., and Coauthors, 1973: Measurements of wind-wave growth and swell decay during the Joint North Sea Wave Project (JONSWAP). *Dtsch. Hydrogr. Z.*, **A8** (Suppl.), 1–95.
- Holthuijsen, L. H., N. Booij, and T. H. C. Herbers, 1989: A prediction model for stationary, short-crested waves in shallow water with ambient currents. *Coastal Eng.*, **13**, 23–54.
- Hwang, P. A., and D. W. Wang, 2004: Field measurements of duration-limited growth of wind-generated ocean surface waves at young stage of development. *J. Phys. Oceanogr.*, **34**, 2316–2326.
- Janssen, P. A. E. M., 1989: Wave induced stress and drag of air over sea water. *J. Phys. Oceanogr.*, **19**, 1631–1642.
- , O. Sætra, C. Wettre, H. Hersbach, and J. Bidlot, 2004: Impact of the sea state on the atmosphere and ocean. *Ann. Hydrogr.*, **3**, 3.1–3.23.
- Kitaigorodskii, S. A., 1962: Application of the theory of similarity to the analysis of wind-generated water waves as a stochastic process. *Bull. Acad. Sci. USSR Ser.*, **1**, 73 pp.
- Komen, G. J., L. Cavaleri, M. Donelan, K. Hasselmann, S. Hasselmann, and P. A. E. M. Janssen, 1994: *Dynamics and Modelling of Ocean Waves*. Cambridge University Press, 532 pp.
- Lin, W., L. P. Sanford, and S. E. Suttles, 2002: Wave measurements and modeling in Chesapeake Bay. *Cont. Shelf Res.*, **22**, 2673–2686.
- Longuet-Higgins, M. S., 1952: On the statistical distribution of the heights of sea waves. *J. Mar. Res.*, **11**, 245–266.
- , 1953: Mass transport in water waves. *Phil. Trans. Roy. Soc.*, **A245**, 533–581.
- Masterbroek, C., G. Burgers, and P. A. E. M. Janssen, 1993: The dynamical coupling of a wave model and a storm surge model through the atmospheric boundary layer. *J. Phys. Oceanogr.*, **23**, 1856–1866.
- Mellor, G. L., 2002: The oscillatory bottom boundary layer. *J. Phys. Oceanogr.*, **32**, 3075–3088.
- , 2003: The three-dimensional, current, and surface wave equations. *J. Phys. Oceanogr.*, **33**, 1978–1989.
- , 2005: Some consequences of the three-dimensional current and surface wave equations. *J. Phys. Oceanogr.*, **35**, 2291–2298.
- , 2005: Some consequences of the three-dimensional current and surface wave equations. *J. Phys. Oceanogr.*, **35**, 2291–2298.
- , 2008: The depth-dependent current and wave interaction equations: A revision. *J. Phys. Oceanogr.*, in press.
- , and A. Blumberg, 2004: Wave breaking and ocean surface thermal response. *J. Phys. Oceanogr.*, **34**, 693–698.
- Moon, I.-J., 2005: Impact of a coupled ocean, wave, tide circulation system on coastal modeling. *Ocean Modell.*, **8**, 203–236.
- Ozer, J., R. Padilla-Hernandez, J. Monbaliu, E. A. Fanjul, J. C. C. Albiach, P. Osuna, J. C. S. Yu, and J. Wolf, 2000: A coupling module for tides, surges and waves. *Coastal Eng.*, **41**, 95–124.
- Phillips, O. M., 1977: *The Dynamics of the Upper Ocean*. Cambridge University Press, 336 pp.
- Pierson, W. J., and L. Moskowitz, 1964: A proposed spectral form for fully developed wind seas based on the similarity theory of A. A. Kitaigoradskii. *J. Geophys. Res.*, **69**, 5181–5190.
- Powell, M. D., P. J. Vickery, and T. A. Reinhold, 2003: Reduced drag coefficient for high wind speeds in tropical cyclones. *Nature*, **422**, 279–283.
- Ruessink, B. G., D. J. R. Walstra, and H. N. Southgate, 2003: Calibration and verification of a parametric wave model on barred beaches. *Coastal Eng.*, **48**, 139–149.
- Schwab, D. J., J. R. Bennett, P. C. Liu, and M. A. Donelan, 1984: Application of a simple numerical wave prediction model to Lake Erie. *J. Geophys. Res.*, **89**, 3586–3592.
- Smolarkiewicz, P. K., 1984: A fully multidimensional positive definite advection transport algorithm with small implicit diffusion. *J. Comput. Phys.*, **54**, 325–362.
- Snodgrass, F. E., G. W. Groves, K. Hasselmann, G. R. Miller, W. H. Munk, and W. H. Powers, 1966: Propagation of swell

- across the Pacific. *Philos. Trans. Roy. Soc. London*, **259**, 431–497.
- Stacey, M. W., 1999: Simulations of the wind-forced near-surface circulation in Knight Inlet: A parameterization of the roughness length. *J. Phys. Oceanogr.*, **29**, 1363–1367.
- SWAMP Group, 1985: *Ocean Wave Modeling*. Plenum Press, 256 pp.
- Terray, E. A., M. A. Donelan, Y. C. Agrawal, W. M. Drennan, K. K. Kahma, A. J. W. Williams III, P. A. Hwang, and S. A. Kitaigorodski, 1996: Estimates of kinetic energy dissipation under breaking waves. *J. Phys. Oceanogr.*, **26**, 792–807.
- Tolman, H. L., 1991: A third-generation model for wind waves on slowly varying, unsteady, and inhomogeneous depths and currents. *J. Phys. Oceanogr.*, **21**, 782–797.
- , and D. Chalikov, 1996: Source terms for a third-generation wind wave model. *J. Phys. Oceanogr.*, **26**, 2497–2518.
- WAMDI Group, 1988: The WAM model—A third generation ocean wave prediction model. *J. Phys. Oceanogr.*, **18**, 1775–1810.
- Xie, L., K. Wu, L. Pietrafesa, and C. Zhang, 2001: A numerical model of wave-current interaction through surface and bottom stresses: Wind-driven circulation in the South Atlantic Bight under uniform winds. *J. Geophys. Res.*, **106** (C8), 16 841–16 855.
- Yin, X.-Q., and L.-Y. Oey, 2007: Bred-ensemble ocean forecast of Loop Current and Rings. *Ocean Modell.*, **17**, 300–326.
- Young, I. R., 2006: Directional spectra of hurricane wind waves. *J. Geophys. Res.*, **111**, C08020, doi:10.1029/2006JC003540.
- Zhang, M. Y., and Y. S. Li, 1997: The dynamic coupling of a third-generation wave model and a 3D hydrodynamic model through boundary layers. *Cont. Shelf Res.*, **17**, 1141–1170.